

MEASURING DUST PRODUCTION IN THE SMALL MAGELLANIC CLOUD CORE-COLLAPSE SUPERNOVA REMNANT 1E 0102.2–7219

KARIN M. SANDSTROM¹, ALBERTO D. BOLATTO², SNEŽANA STANIMIROVIĆ³, JACCO VAN LOON⁴ AND J. D. T. SMITH⁵

¹Astronomy Department, 601 Campbell Hall, University of California, Berkeley, CA 94720, USA

²Department of Astronomy and Laboratory for Millimeter-wave Astronomy, University of Maryland, College Park, MD 20742, USA

³Department of Astronomy, University of Wisconsin, Madison, WI 53706, USA

⁴Astrophysics Group, Lennard-Jones Laboratories, Keele University, Staffordshire ST5 5BG, UK and

⁵Ritter Astrophysical Research Center, University of Toledo, OH 43603, USA

Submitted to ApJ.

ABSTRACT

We present mid-infrared spectral mapping observations of the core-collapse supernova remnant 1E 0102.2–7219 in the Small Magellanic Cloud using the InfraRed Spectrograph (IRS) on the Spitzer Space Telescope. The remnant shows emission from fine structure transitions of neon and oxygen as well as continuum emission from dust. Comparison of the mid-IR dust emission with observations at x-ray, radio and optical wavelengths shows that the dust is associated with the supernova ejecta and is thus newly formed in the remnant. The spectrum of the newly formed dust is well reproduced by a model that includes $3 \times 10^{-3} M_{\odot}$ of amorphous carbon dust at 70 K and $2 \times 10^{-5} M_{\odot}$ of Mg_2SiO_4 (forsterite) at 145 K. Our observations place a lower limit on the amount of dust in the remnant since we are not sensitive to the cold dust in the unshocked ejecta. We compare our results to observations of other core-collapse supernovae and remnants, particularly Cas A where very similar spectral mapping observations have been carried out. We observe a factor of ~ 10 less dust in E0102 than seen in Cas A, although the amounts of amorphous carbon and forsterite are comparable.

Subject headings: dust, extinction — infrared: ISM — supernova remnants

1. INTRODUCTION

Dust is a crucial component of the interstellar medium (ISM). It provides a site for interstellar chemistry, in particular the formation of molecular hydrogen; it regulates thermal balance in various phases of the ISM; and it provides shielding for dense clouds, critically influencing the process of star-formation. The characteristics of interstellar dust depend on the balance between its formation and destruction and on the processing that dust grains endure in the ISM. The mechanisms for dust production, their timescales and efficiencies and the effect of metallicity on these quantities determine the cosmic history of dust production and are mostly not well characterized.

In particular, the relative amount of dust that core-collapse supernovae (CCSN) contribute to the ISM is poorly constrained and a matter of much debate. Because of the short lifetimes of their massive progenitor stars (a few tens of Myrs), CCSN are often cited as an important source of dust early in the history of the Universe (Morgan et al. 2003; Dwek et al. 2007; Todini & Ferrara 2001). Observational evidence for substantial dust production in supernovae, however, is scant and controversial.

Our understanding of dust formation in the early Universe and the role of CCSN has recently been challenged by observations of large dust masses around high redshift quasars (Bertoldi et al. 2003; Beelen et al. 2006). Because the redshifts of these quasars are so high and the dust masses are so large, the dust had to be produced efficiently and on a short timescale. For the $z = 6.42$ quasar SDSS J1148+5251, the age of the Universe is only ~ 900 Myr and more than $10^8 M_{\odot}$ of dust are observed in its vicinity (although there are substantial

uncertainties associated with this dust mass, see the discussion in Omont et al. (2001)). There is some indication that dust in some of these high redshift galaxies may follow an extinction curve unlike that in either the Milky Way or Small Magellanic Cloud (Maiolino et al. 2004). Hirashita et al. (2005) claim that the extinction curve of dust in the $z = 6.19$ quasar SDSS J1048+4637, for example, can be reproduced by the species and size distribution of dust formed in models of the unmixed ejecta of $\sim 10 - 30 M_{\odot}$ supernovae.

The models of dust production in supernovae typically predict on the order of $0.1 - 1 M_{\odot}$ of dust formed in an average CCSN (see for instance, Todini & Ferrara 2001; Nozawa et al. 2003). Dwek et al. (2007) estimate that to produce the mass of dust observed around SDSS J1148+5251 requires an average yield of $\sim 1 M_{\odot}$ of dust per CCSN. As of yet, however, observations of newly-formed dust in supernovae and their remnants have shown orders of magnitude less dust than would be expected based on these models. If we cannot substantiate the predicted dust production efficiency of CCSN, our explanation of the high- z quasar observations may need to rely more heavily on the contributions of red supergiants and massive AGB stars to dust production (van Loon et al. 2005, 2008).

Part of the discrepancy between expectations and observations of dust production in CCSN and their remnants stems from the difficulty of observing newly-formed dust. The condensation of dust is thought to happen between $\sim 400 - 800$ days after the explosion (Kozasa et al. 1989; Todini & Ferrara 2001; Nozawa et al. 2003). While the newly-formed dust is still warm, its near- and mid-IR emission may be detectable. Observations of the thermal emission newly-formed from dust in SN 1987A show $\sim 10^{-4} M_{\odot}$ of dust produced by 775 days after

the explosion (Roche et al. 1993; Wooden et al. 1993; Moseley et al. 1989). Sugerman et al. (2006) claimed to detect mid-IR emission from $\sim 0.02 M_{\odot}$ of newly-formed dust in SN 2003gd, although this claim has been disputed by Meikle et al. (2007) after their reanalysis of the Spitzer observations that showed only $4 \times 10^{-5} M_{\odot}$ of dust. At these early times, near- and mid-IR emission can also arise from IR light echoes, as the supernova’s radiation heats pre-existing circumstellar dust (Bode & Evans 1980; Dwek 1983; Pozzo et al. 2004). If there is a contribution by an IR light echo, the mass of newly-formed dust inferred from the early-time infrared emission may be greatly overestimated. On the other hand, clumpiness of the ejecta could lead to an underestimate of the dust mass based on the infrared emission (Ercolano et al. 2007).

As the supernova ejecta expand and cool, the newly-formed dust becomes detectable only at far-IR and/or submillimeter wavelengths at which time confusion with cold dust in nearby star-forming regions becomes a major issue. Dunne et al. (2003) claimed a detection of $\sim 2 M_{\odot}$ of newly-formed dust in Cas A with $850 \mu\text{m}$ SCUBA observations. Krause et al. (2004), however, used far-IR and molecular line observations to argue that there is at least an order of magnitude less newly-formed dust in Cas A and that most of the submillimeter emission arises in an intervening molecular cloud. Similarly, submillimeter observations of Kepler’s remnant were used by Morgan et al. (2003) to argue for $0.1 - 3 M_{\odot}$ of newly-formed dust although these results have been recently disputed by Blair et al. (2007) who find evidence for only $5 \times 10^{-4} M_{\odot}$ using far-IR observations from Spitzer.

Eventually, the interaction of the ejecta with the surrounding circumstellar and/or interstellar medium (CSM/ISM) produces a reverse shock which propagates back into the ejecta. The reverse shock reheats the newly-formed dust so that once again it is detectable in the mid-IR and may destroy some of the dust via sputtering, as well. Observations at $24 \mu\text{m}$ of 1E0102.2–7219, the same SNR we discuss here, by Stanimirović et al. (2005) showed evidence for $\sim 8 \times 10^{-4} M_{\odot}$ of dust. Recently, Rho et al. (2008) used IRS on Spitzer to make a spectral map of Cas A. They claim evidence for $\sim 0.02 M_{\odot}$ of newly-formed dust in the remnant. Since only the reverse-shocked dust should be visible in the mid-IR, only a fraction of the newly-formed dust can be detected in this way. Additionally, circumstellar or interstellar dust that is interacting with the forward shock should also be detected in the mid-IR. Williams et al. (2006) observed four supernova remnants in the Magellanic Clouds with the IRAC and MIPS instruments on Spitzer and concluded that the mid-infrared emission was from shocked circumstellar dust rather than newly-formed dust. Despite these limitations mid-IR observations are very useful for studying the dust production in supernovae because they typically have higher angular resolution, which allows the remnant to be more easily separated from foreground and background emission. Mid-IR spectroscopy also has the potential to provide some information on the composition of the newly-formed dust in a remnant from the distinctive mid-IR spectral features of some dust species. In this paper we present mid-IR spectral mapping observations of the Small Magellanic Cloud remnant 1E0102.2–7219, which

we use to learn about the mass and composition of dust produced in CCSN.

SNR 1E0102.2–7219 (E 0102) is a young, oxygen-rich remnant located on the outskirts of the emission-line nebula N 76. It is thought to be the product of a Type Ib/Ic or IIL/b supernova (Blair et al. 2000; Chevalier 2005) due to the lack of hydrogen and helium in the remnant’s spectrum and the high abundance of oxygen and neon in its ejecta. E 0102 has been observed extensively at x-ray, UV, optical, infrared and radio wavelengths. Chandra x-ray imaging of the remnant by Gaetz et al. (2000) showed a textbook remnant structure with a blast wave radius of $\sim 22''$ and a reverse shock radius of $\sim 15''$. Amy & Ball (1993) observed the remnant at 6 cm using the Australia Telescope Compact Array (ATCA) and found a shell of radio emission with a radius of $\sim 20''$. This ring lies between the measured radii of the faint rim of the blast wave and the bright ring of the reverse shock, and is attributed to material in the forward shock. The full-width velocity dispersion of the optical [O III] emission from the remnant was measured to be $\sim 6000 \text{ km/s}$ by Tuohy & Dopita (1983), implying an age of ~ 1000 years given the remnant’s size. Hughes et al. (2000) use three epochs of x-ray observations from the *Einstein*, *ROSAT* and *Chandra* observatories to measure an expansion rate for the whole remnant in agreement with the results of Tuohy & Dopita (1983). Recent work by Finkelstein et al. (2006) used two epochs of optical [O III] observations to determine proper motions for ejecta filaments and find an age of 2050 ± 600 years for the remnant. The results of the following work do not depend sensitively on the age, so we adopt a value of 1000 years for simplicity.

Stanimirović et al. (2005) presented the first infrared detection of SNR E 0102 from the Spitzer Survey of the Small Magellanic Cloud ($S^3\text{MC}$) observations. $S^3\text{MC}$ covered the star-forming regions of the SMC Bar and Wing with imaging in all MIPS and IRAC bands (Bolatto et al. 2007). The remnant was only clearly detected at $24 \mu\text{m}$. Stanimirović et al. (2005) used the $24 \mu\text{m}$ detection along with the upper limits in the other bands to argue that the dust in the remnant has a temperature of $\sim 120 \text{ K}$ and they determined an upper limit of $8 \times 10^{-4} M_{\odot}$ of warm dust. The main uncertainties in their analysis were the fraction of the MIPS $24 \mu\text{m}$ emission coming from the [O IV] line at $24.8 \mu\text{m}$ and the temperature of the dust.

In the following, we present Spitzer IRS spectral mapping observations of SNR 1E0102.2–7219 obtained as part of the Spitzer Spectroscopic Survey of the Small Magellanic Cloud ($S^4\text{MC}$). These observations allow us to map the emission lines and dust continuum from the remnant and place a lower limit on the amount of newly formed dust in E 0102. In Section 2.1 we describe the observations and their reduction. In Section 3.1 we present the spectrum of the remnant and discuss the spatial distribution of its various components. In Section 3.3 we use a model for the reverse-shocked dust to measure a mass of $3 \times 10^{-3} M_{\odot}$ and we discuss the composition of the dust as revealed by its spectrum. Section 4 discusses the implications of our measurement for the understanding of CCSN dust production and compares our results with previous work.

2. OBSERVATIONS AND DATA REDUCTION

2.1. *Spitzer Observations*

SNR E 0102 was mapped with all LL and SL orders of IRS on the Spitzer Space Telescope as part of the S⁴MC project (Spitzer Spectroscopic Survey of the Small Magellanic Cloud, GO 30491). The wavelength coverage of the SL and LL orders extends from 5.2 to 38.0 μm with a spectral resolution between 60 and 120. Ramp times of 14 and 30 seconds for SL and LL were chosen as a compromise between sensitivity, spatial coverage and observation length.

SNR E 0102 was covered in the spectral maps of the N76 region, observed on 9 and 12 December 2006 for SL and LL, respectively. The LL map consists of 6×75 pointings covering an area of 474×381 arcseconds² in both LL1 and LL2. The SL observations consisted of 5×120 pointings covering 260×222 arcseconds² for the SL1 and SL2 orders. The roll angle was left unconstrained for our observations. The SL and LL maps have different orientations because of the slit positions in the focal plane of the telescope. Figure 1 shows a three-color image of the region from the S³MC dataset overlaid with the coverage of the SL2, SL1, LL2 and LL1 maps. The spectral maps are completely sampled in both LL and SL by stepping perpendicular to the slit by one-half slit width (5.08 and 1.85" for LL and SL, respectively). In the SL orders we have stepped by a full slit width parallel to the slit (52") in order to increase the spatial coverage of the maps at the expense of some redundancy. In the LL orders we have used half-slit width steps parallel to the slit (79"). More redundancy in the LL maps is necessary due to the increasingly large numbers of bad pixels at long wavelengths.

2.2. *Data Reduction*

The spectral maps were calibrated and assembled in IDL using the Cubism package (Smith et al. 2007). Cubism takes as input pipeline-processed two-dimensional spectral images from IRS and produces three dimensional spectral data cubes using a reprojection algorithm which employs two steps of polygon clipping (in which the exact geometrical overlap of input pixels, or pseudo-rectangles in the case of the IRS spectral images, is used to calculate its weight in an output pixel grid). Cubism also applies an aperture loss correction function (ALCF) and a slit loss correction function (SLCF) to adjust the calibration which is based on point-source observations rather than extended sources. The output pixel scales of the LL and SL cubes are 5.08" and 1.85", respectively. Images of the IRS data in this work are shown on the IRS pixel scale rather than aligned to R.A. and Dec to avoid unnecessary interpolation.

The Galactic and zodiacal light foregrounds were removed from the IRS spectra using a dedicated "off" position. The same position was used for both the LL and SL modules. The background observations were done immediately following the mapping observations. The "off" position was chosen as a place in the S³MC 24 μm MIPS mosaic with no extended emission or point sources, located at R.A. 1^h09^m40^s.00, Dec. $-73^\circ 31' 30''$.00.

The subtraction of the "off" position, in addition to removing the Galactic and zodiacal foregrounds, mitigates the effects of rogue pixels (i.e. time variable bad pix-

els) in the IRS detectors, although it does not eliminate them. Further bad pixel removal was done in Cubism by examining each wavelength for striping (caused by global bad pixels) and other artifacts. The effect of bad pixels increases at the longer wavelengths, degrading the data quality beyond about 35 μm .

2.3. *Resolution Matching and Alignment of Cubes*

In order to directly compare the spatial distribution of supernova emission at each wavelength as well as properly extract a spectrum when the extraction region is on the order of a resolution element, it was necessary to convolve all the individual slices of the spectral cube to the same resolution. This was achieved by creating convolution kernels based on theoretical point-spread functions (PSFs) for the IRS spectrograph generated by the program sTinyTim¹.

The convolution kernels k were defined in the following way:

$$k = \text{FFT}^{-1}(R/I), \quad (1)$$

where R is the 2-dimensional Fast Fourier Transform (FFT) of the PSF of the longest wavelength slice of the LL1 cube and I is the FFT of the PSF of the slice in question. The convolution kernels were masked in Fourier space such that there was no power at spatial frequencies higher than the Nyquist frequency of the lowest resolution kernel in order to avoid the amplification of high-frequency noise. Each slice of the spectral data cube was then convolved with the appropriate kernel. Although the PSF of IRS is not well explored (i.e. the predictions from sTinyTim are mostly untested) and the PSF that Cubism recovers can be somewhat elongated in a way that varies with wavelength, we found that the results of this technique were adequate for our purposes. The convolution process was tested on the cube of the N 22 region of the SMC which contains a very bright point source for which the first two diffraction rings are visible for essentially every slice in the cube from SL2 through LL1. The correspondence between wavelength slices after our convolution is excellent as shown in Figure 2. For each cube, the associated uncertainty cube was also convolved and the errors appropriately propagated.

The LL1, LL2, SL1 and SL2 cubes were aligned using a technique based on the polygon-clipping algorithm implemented in Cubism. In polygon-clipping the weight assigned to each pixel in the original image is calculated based on the geometric overlap of that pixel with the grid of output pixels. Aligning the cubes using polygon clipping minimizes interpolation error and allows for direct propagation of the associated uncertainty cubes. The LL2, SL1 and SL2 cubes were aligned to match the astrometry and pixel scale of the LL1 map after resolution matching.

2.4. *Local Background Removal*

More difficult to remove than the Galactic foreground is the variable and complex local foreground and background emission (for simplicity we will refer to this as a background, though there are contributions from the entire line of sight through the SMC). E 0102 is located near the large emission-line complex N 76. Emission from the

¹ <http://ssc.spitzer.caltech.edu/archanalyst/contributed/stinytim/index>

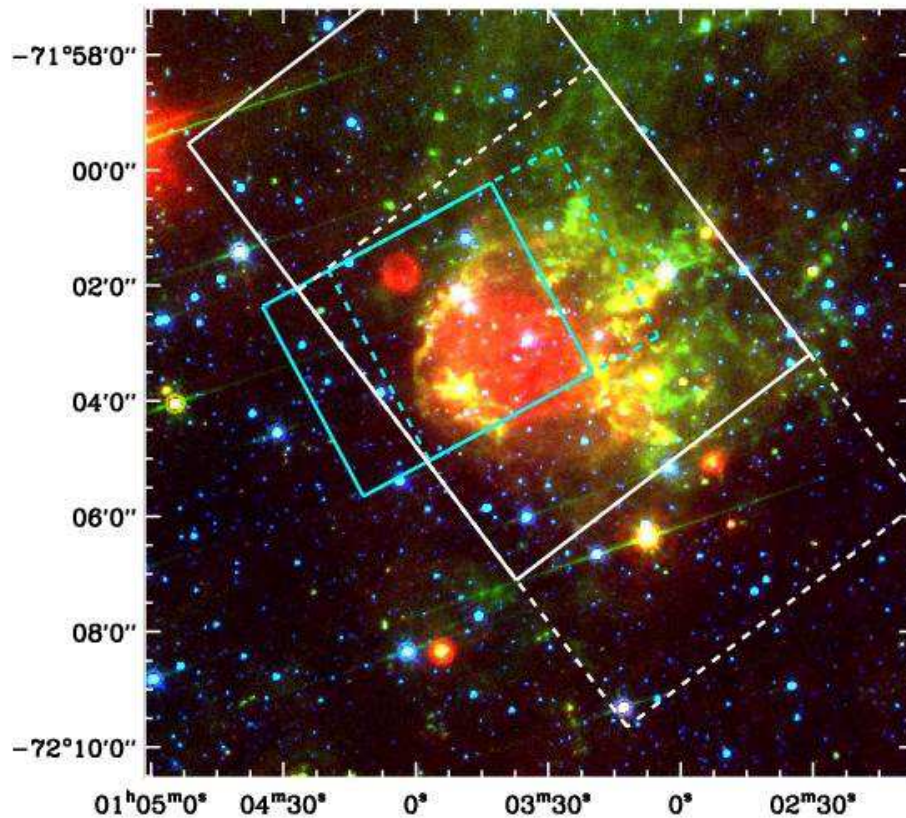


FIG. 1.— Three-color image of the N 76 region overlaid with the coverage of the IRS spectral mapping observations. The S^3MC MIPS and IRAC maps at 24, 8.0 and $3.6\ \mu m$ are shown in red, green and blue. The white solid and dashed lines show the coverage of the LL1 and LL2 spectral maps. The cyan solid and dashed lines show the coverage of the SL1 and SL2 maps. The 1E0102.2–7219 supernova remnant is located at R.A. $01^h04^m02^s.1$, Dec. $-72^\circ01'52''.5$ (J2000).

outskirts of this region must be removed from the supernova remnant spectrum to accurately measure the dust content and emission line flux.

An accurate background subtraction is not possible over a large area due to the proximity of N 76 and the complexity of the emission in the region. For this reason we focus on the area near the supernova remnant and attempt to subtract a model for the local emission. We first attempted to fit planar or higher order surfaces to the emission in the region of the remnant. The steep profile on the side of N 76 nearest the remnant was poorly represented in these fits, resulting in large residuals. Polynomial fits to each row and column, as done by Stanimirović et al. (2005), were a better representation of the local emission but also suffered from issues with reproducing the steepness of the N 76 shoulder, interfering with the goal of determining the background in the immediate vicinity of the remnant. Rather than trying to reproduce the local emission we argue that a better representation of the background comes from interpolating across the supernova remnant, which eliminates the need to reproduce the complex emission structures with polynomials or surfaces.

For each slice of the convolved and aligned cubes, we mask out the immediate region of the remnant, using

a mask $60''$ in diameter to exclude any emission from the remnant in our background determination. We then linearly interpolate in the x and y directions across the masked region, using two pixels on either side of the remnant in the given row or column. Finally, we average together the results obtained by interpolating in the x and y direction. This technique has advantages and disadvantages. Since we only use the four pixels nearest the remnant, there is some random noise in the background value. We believe this disadvantage is far outweighed by the difficulty in doing any kind of more complex fit given the spatial intensity variations of the background. In addition, the column based interpolation also tends to remove any residual striping in the LL cubes that results from the effects of rogue detector pixels.

A plot of the background spectrum is shown in the bottom panel of Figure 3. Subtracting the background eliminates the contributions of [S III], [Si II] and PAHs entirely from the SNR spectrum showing that emission from these species is not related to the remnant. All of these emission features are typical for the ISM irradiated by the average interstellar radiation field (ISRF). The local background spectrum is slightly negative at short wavelengths. This is most likely due to the gradient in the zodiacal and Galactic foregrounds between the

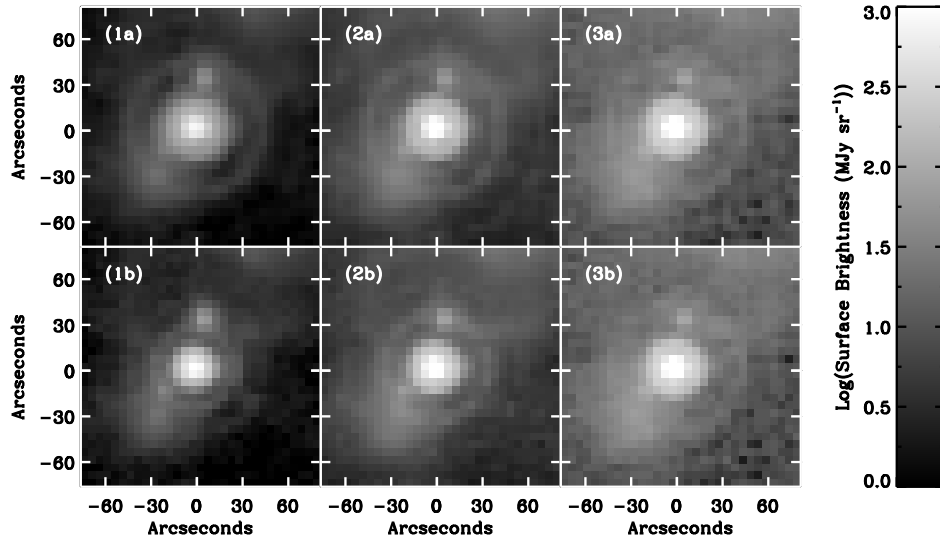


FIG. 2.— Results of the convolution described in Section 2.3 for a bright point source in the N 22 region. The panels show the point source at (1) 23.0 μm , (2) 30.0 μm , and (3) 36.7 μm . The bottom panels (1b), (2b) and (3b), show the point source before the convolution. The top panels, labeled (1a), (2a) and (3a) show the source after convolution. The image stretch is logarithmic to highlight the faint diffraction rings around the point source. After the convolution, the diffraction rings are aligned at all wavelengths, showing the effectiveness of our sTinyTim derived convolution kernels.

location of the dedicated “off” position and the remnant. Subtracting the local background, however, corrects for this over-subtraction in the spectrum of the remnant. In the continuum, background emission accounts for 40 to 60% of the emission. For the emission lines, the background subtraction removes a few percent of the integrated strength of [Ne III] and [O IV].

In general, the local emission in each wavelength slice has a very similar spatial structure, except at the wavelengths of strong emission lines. In the strong emission line from [O IV] and/or [Fe II] at 25.8 μm , a diffuse halo is evident around the supernova remnant. This ionized gas cannot be from material that is collisionally interacting with the remnant since it is well outside the extent of the forward shock. A similar structure is seen at the wavelengths of the other spectral lines. The ionized material surrounding the remnant has been observed previously in optical studies (Tuohy & Dopita 1983; Blair et al. 2000; Finkelstein et al. 2006). The source of the ionization for this surrounding material has been discussed by Tuohy & Dopita (1983). It is possible that the material was ionized by the supernova shock breakout or is currently being ionized by emission from the radiative shocks in dense knots of ejecta in E 0102. The surroundings of the remnant will be discussed further in Section 4.5.

3. ANALYSIS

3.1. The Mid-IR Spectrum

3.1.1. Sources of Dust Continuum Emission

We now consider the possible sources for dust continuum emission from SNR E 0102: circumstellar/interstellar dust in the forward shocked region, newly formed dust in the reverse shocked ejecta or newly formed dust in the unshocked ejecta. The contribution of each of these regions to the spectrum depends on the mass, temperature and composition of the dust present.

The dominant heating process for dust in the shocked ejecta and shocked CSM/ISM will be collisions with electrons (Dwek & Werner 1981; Arendt et al. 1999). The equilibrium temperature of a dust grain that is collisionally heated in a plasma can be found by equating the collisional heating rate of the grain with its radiative cooling rate. The collisional heating rate for a dust grain with size a by particles with mass m , density n and temperature T is given by Dwek (1987):

$$H(a, T, n) = (32/\pi m)^{1/2} \pi a^2 n (kT)^{3/2} h(a, T). \quad (2)$$

Here $h(a, T)$ is a dimensionless parameter which describes the grain “heating efficiency” and depends on the fractional amount of the incident energy of the particle that is deposited in the grain by the collision. Dwek (1987) develop an approximation for $h(a, T)$ based on a comparison of the effective thickness of the grain $4a/3$ and the experimentally measured stopping distance of an electron or ion in a solid. We use their formulae in this analysis. The radiative cooling rate of the grain is given by:

$$L_{gr}(a, T_d) = 4\pi a^2 \sigma T_d^4 \langle Q(a, T_d) \rangle, \quad (3)$$

where $\langle Q(a, T_d) \rangle$ is the Planck-averaged value of the absorption coefficient for a dust grain of the given size and temperature. Equating these heating and cooling rates yields the equilibrium temperature of the grain.

In the remnant, shocked CSM/ISM dust would be located in a shell with an outer radius of 22” and an inner radius at the contact discontinuity, the exact position of which has not been determined. X-ray spectroscopy of the blast wave region shows post-shock material with abundances consistent with the SMC, electron temperatures around 1 keV, and ionization timescales $\tau = n_e t \sim 3 \times 10^{10} \text{ s cm}^{-3}$ (Hayashi et al. 1994; Hughes et al. 2000; Sasaki et al. 2006). Assuming a timescale of ~ 1000 years (the age of the remnant) gives electron densities in the forward shock region of $n_e \sim 1 \text{ cm}^{-3}$. Collisionally

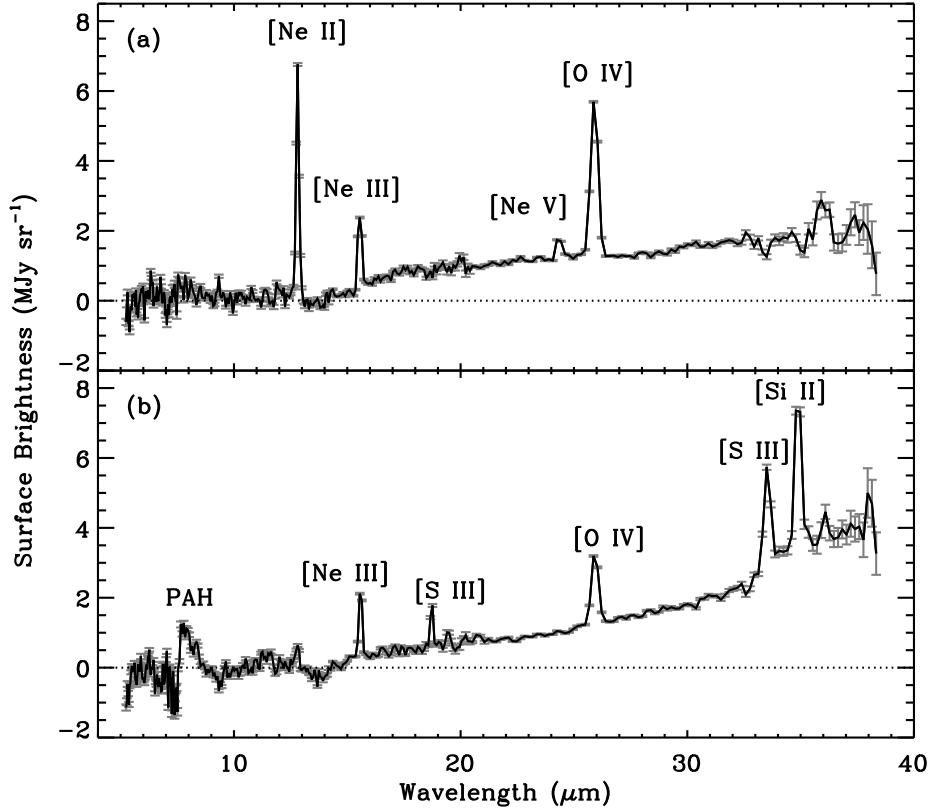


FIG. 3.— This figure shows (a) the spectrum of SNR E 0102 after the subtraction of the local background and (b) the local background spectrum. The spectrum of the supernova remnant shows dust continuum and emission lines from neon and oxygen. The background spectrum shows lines from sulfur, silicon, neon and oxygen as well as emission from polycyclic aromatic hydrocarbons around $8\ \mu\text{m}$ and dust continuum. The contributions from silicon, sulfur and PAHs are entirely removed from the remnant's spectrum after background subtraction. The background spectrum is slightly negative at short wavelengths due to oversubtraction of the Galactic and zodiacal light foregrounds. The background subtraction corrects this oversubtraction in the spectrum of the remnant.

heated dust grains in this region would have equilibrium temperatures of between 30 and 70 K for silicate and carbonaceous grains with sizes between 0.001 and $1.0\ \mu\text{m}$ (assuming the optical constants for interstellar graphite and silicate grains from Laor & Draine 1993). Figure 4 shows the equilibrium temperature of dust grains in the forward shocked plasma as a function of grain size. The collision rates in this plasma, as well as in the reverse shock, are low enough that the grains are not heated above their sublimation temperature and destruction of the grains via evaporation.

Shocked ejecta dust would be located in a shell with an outer radius at the contact discontinuity and an inner radius at $15''$. The heating mechanism of the dust in the shocked ejecta depends on its density structure. When the reverse shock encounters more diffuse parts of the ejecta its passage creates hot x-ray emitting plasma. X-ray spectroscopy of the shocked ejecta shows a plasma composed of oxygen, neon, magnesium and silicon with electron temperatures around $0.4\ \text{keV}$ ($5 \times 10^6\ \text{K}$) and ionization timescales of $n_e t \sim 10^{12}\ \text{s cm}^{-3}$. Assuming $t \sim 1000$ years, as before, gives densities in the x-ray emitting reverse shocked ejecta of $\sim 20\ \text{cm}^{-3}$. Figure 4 also shows the equilibrium temperature of collisionally heated amorphous carbon and forsterite (Mg_2SiO_4) grains as a function of size given these plasma parameters, using optical constants from Rouleau & Martin (1991) for amorphous carbon and Jäger et al. (2003) for

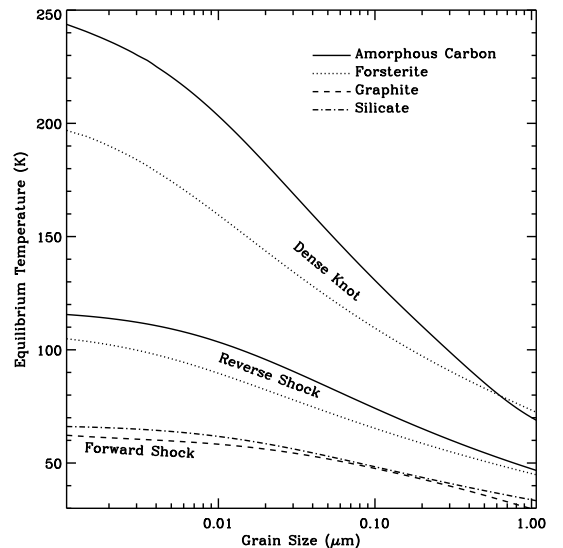


FIG. 4.— The equilibrium temperature of collisionally heated grains of different compositions in the forward and reverse shocked x-ray emitting plasma and the hot, post-shock region of a dense knot. We plot only amorphous carbon and forsterite in the reverse shocked ejecta based on the results of our dust model fits in Section 3.4. We assume that dust grains in the shocked CSM/ISM will have the optical properties characteristic of interstellar graphite and silicate from Laor & Draine (1993).

forsterite and assuming the heating efficiencies for carbonaceous and silicate dust from Dwek (1987).

The interaction of the reverse shock with material in dense clumps of ejecta drives radiative shocks that produce optical and infrared line emission, discussed further in Section 3.1.2, and heat the dust grains by a combination of radiative and collisional processes. Arendt et al. (1999) compared the collisional and radiative heating for dust in the hot, post-shock region of a knot in Cas A assuming the density, temperature and cooling function predicted by the models of Sutherland & Dopita (1995) for shock velocities between 150–200 km s^{−1}—the same models which are found to best reproduce the optical and UV emission from E 0102. They found that the collisional heating exceeds radiative heating under these conditions by factors of a few hundred. Thus, for dust in the immediate post-shock part of dense knots, we can ignore radiative heating. Figure 4 shows the equilibrium temperatures for collisionally heated dust grains in this region, using $T_e = 10^{6.64}$ K, $n_e = 400$ cm^{−3} and the gas cooling function $\Gamma = 10^{-17.5}$ ergs cm³ s^{−1} from Sutherland & Dopita (1995). On the other hand, in the cooled post-shock gas of the dense knots and the in cold pre-shock gas, the dust is likely heated by the radiation field generated by the shock front. Bouchet et al. (2006) calculate the radiative heating for dust in similar conditions in SN 1987A and find that it can reach temperatures of ~ 125 K. Given the angular resolution of our observations we will not be able to distinguish regions where dust in knots is collisionally or radiatively heated, but we note that the equilibrium dust temperatures in these circumstances are all between ~ 100 –200 K.

If the dust grains in these various collisionally heated regions are small enough, a collision with a single electron may be sufficient to raise the grain temperature well above the equilibrium value for a short time. After this temperature spike the grain can cool to below the equilibrium temperature, resulting in a large range of temperatures for a given grain size. An important consideration when dealing with this stochastically heated dust is that only some fraction of the grains will be warm at a given time, so our mid-IR observations may miss a substantial fraction of the dust. Grains will be stochastically heated in this manner when two conditions are met: 1) the collisional rate is slow compared with the cooling rate of the grain and 2) the amount of energy deposited by a single electron is large compared with the internal energy of the grain.

For the plasma conditions in the forward and reverse shocks, Figure 5 shows the ranges of grain size for which we expect the dust to be in equilibrium with the plasma based on the ratios between the energy deposited by one electron and the grain’s total internal energy ($\Delta E/U$) and the ratio between the cooling time and collision time (τ_{cool}/τ_{coll}). For simplicity we show only one grain species for the forward and reverse shocks: graphite in the forward shock and amorphous carbon in the reverse shock. The size at which equilibrium is reached is a factor of ~ 2 smaller for silicate grains in the forward shock and a factor of ~ 1.5 smaller for forsterite grains in the reverse shock. For this calculation we have used the heat capacity of graphite grains from Dwek (1986) and silicate from Draine & Anderson (1985), both of which are based on fits to experimental data, and the same optical

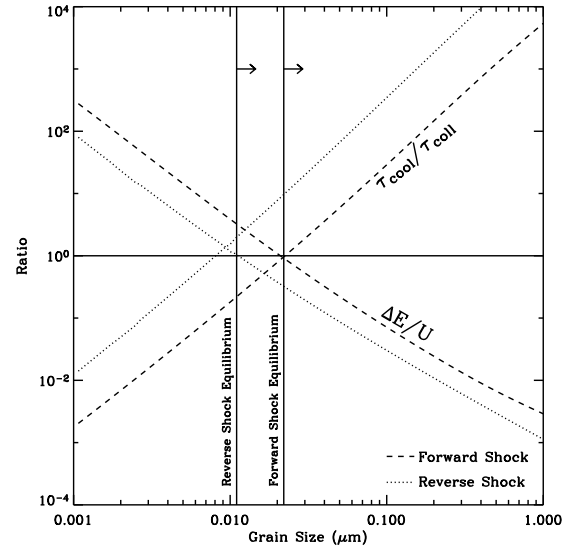


FIG. 5.— This plot illustrates the range of dust grain sizes that will be in equilibrium in the forward and reverse shocks. The dotted lines are for amorphous carbon in the reverse shock and the dashed lines are for graphite in the forward shock, assuming the densities and temperatures discussed in the text. Two ratios are shown on the plot: the ratio between the cooling time and the collision time (τ_{cool}/τ_{coll}) and the ratio between the energy deposited by a collision with one electron and the internal energy of the grain ($\Delta E/U$). When the ratio of the collision time to the cooling time is large (i.e. collisions happen faster than the dust grain can cool) and the ratio of the energy deposited by one electron to the total internal energy of the grain is small (i.e. the grain temperature does not change appreciably from one collision) then the grains can be said to be in equilibrium. The grain size for which these conditions are met are > 0.01 μm for amorphous carbon in the reverse shock and > 0.02 μm for graphite in the forward shock. This size is a factor of ~ 1.5 smaller for forsterite in the reverse shock and ~ 2 smaller for silicate dust in the forward shock.

constants used in Figure 4. The graphite heat capacity is used for amorphous carbon and the silicate heat capacity is used for forsterite. For the estimates presented here, this level of accuracy should be sufficient, though the heat capacity of a dust grain does depend on its composition, shape and “fluffiness” among other factors.

The unshocked ejecta are located inside the reverse shock radius of $15''$. The density, temperature and structure of the unshocked ejecta are unobserved. We can place limits on the temperature of the gas and dust by considering the processes responsible for heating and cooling the ejecta. In the initial phases of the remnant’s expansion the ejecta are heated by the decay of radioactive isotopes produced in the explosion. As the remnant expands, the ejecta cool adiabatically, reaching a temperature cool enough to allow dust condensation after about 400 to 800 days post-explosion (Todini & Ferrara 2001; Nozawa et al. 2003). Assuming adiabatic cooling with an index $\gamma = 1.25$ as used by Kozasa et al. (1989) and a temperature of ~ 1000 K 400 days after the supernova, the current gas temperature would be less than the temperature of the cosmic microwave background. Before reaching that temperature, of course, the dust and gas would come into equilibrium with the local radiation field which has contributions from both the general SMC radiation field and the emission from E 0102’s shock fronts. The equilibrium temperature of big grains in the interstellar radiation field of the SMC is ~ 20 K (Bot et al.

2004; Leroy et al. 2007), so we consider this a lower limit on the temperature of the unshocked ejecta dust.

3.1.2. *Oxygen and Neon Fine-Structure Emission Lines*

We observe emission from fine-structure transitions of [Ne II], [Ne III], [Ne V] and [O IV] in the mid-IR spectrum of E 0102. At the spectral resolution of the LL1 order, the [O IV] line overlaps with [Fe II] at 25.988 μm . However, given the predominance of oxygen in the supernova remnant as observed in the optical, x-ray and UV and the dearth of iron emission observed at any wavelength, we consider it very likely that the 25.8 μm emission line is due to [O IV]. Table 1 lists the detected emission lines and their strengths. Examination of the spatially resolved velocity information shows a range of velocities in agreement with previous spectroscopic measurements of optical line emission.

The contribution of [O IV] to the 24 μm flux was one of the major uncertainties for Stanimirović et al. (2005) in their analysis of the mass of newly formed dust in the remnant. We find that [O IV] is responsible for $\sim 15\%$ of the 24 μm flux from the remnant, significantly less than the 60% they were forced to assume due to the lack of spectroscopic information.

The line emission from oxygen-rich supernova remnants like E 0102 is thought to arise from slower, radiative shocks created when the reverse shock encounters dense clumps of ejecta. Due to the high abundance of oxygen and other heavy elements in the nuclear-processed stellar ejecta, the cooling time behind these shocks is shorter than the recombination time, producing a plasma that is much cooler than its ionization state would indicate. The relative ionization levels in the post-shock ejecta depend upon the details of the shock front and the ionization state of the material prior to encountering the reverse shock. Sutherland & Dopita (1995) found that the optical emission spectrum of E 0102 could be fit relatively well with a model for the reverse shock entering a dense ejecta knot with velocities between 150 and 200 km s^{-1} and creating a precursor photoionization front that determines the initial ionization state of the pre-shock gas. Using the observed mid-IR emission line strengths to determine physical conditions in the ejecta would require shock modeling outside the scope of this paper.

3.2. *Spatial Decomposition of the Mid-IR Emission*

At the resolution and signal-to-noise of our observations it is difficult to spatially separate the emission from circumstellar/interstellar dust in the forward shock from the emission from newly formed dust heated by the reverse shock. The outer radius of the forward shock, as measured by Gaetz et al. (2000) is $\sim 22''$ while the inner radius of the reverse shock is $\sim 15''$. In between, the two plasmas are separated by a contact discontinuity, the location of which has not been measured. The resolution of the IRS instrument in the LL1 order ranges between 6 and 9'' and the pixel scale is $\sim 5''$. The angular resolution inhibits our ability to separate newly formed dust from dust heated by the forward shock, without more detailed modeling. Measuring the amount of forward shocked dust is also an interesting quantity on its own (Section 4.5).

The close correspondence between the 0.3 – 10 keV Chandra map and the 24 μm dust map, as noted by Stanimirović et al. (2005), suggests that the dust emission is mainly from the reverse shocked material and is thus newly formed in the remnant. In this section, we quantify the fraction of the dust emission at each wavelength in our cube that can be attributed to dust in the ejecta of the supernova by decomposing the remnant spatially using x-ray, radio and optical observations as templates for the sources of emission in the remnant. As discussed in the previous section, there are three mechanisms for which we might expect to detect mid-IR dust emission: CSM/ISM dust in the forward shocked region, newly formed dust in the x-ray emitting regions of reverse shocked gas and newly formed dust in the dense knots of ejecta. This approach is similar to that used by Arendt et al. (1992) in studying dust emission from the Cygnus Loop. We will first discuss the template images we use to represent these three emission mechanisms.

Emission from the forward shocked material can be traced by radio continuum emission. The radio continuum is synchrotron emission from electrons interacting with the compressed CSM/ISM magnetic field in the region between the blast wave and the contact discontinuity. Amy & Ball (1993) observed the remnant at 6 cm using the Australia Telescope Compact Array. They see a shell structure which fills the region between the faint outer boundary of the blast wave as traced by x-ray emission and the outer boundary of the reverse shock. We use the radio map as a tracer of the forward shocked circumstellar and interstellar material.

We have used the 0.3 – 10 keV Chandra x-ray map of Gaetz et al. (2000) to trace the x-ray emitting reverse shocked material. X-ray spectroscopy of E 0102 has demonstrated that the bright x-ray ring contains material composed primarily of oxygen and neon with smaller contributions from magnesium and silicon, consistent with the nucleosynthetic products of a massive star (Flanagan et al. 2004; Sasaki et al. 2006). Finally, to trace the spatial distribution of dust in dense knots of reverse shocked material we use the optical [O III] 5007 Å emission from HST ACS imaging by Finkelstein et al. (2006) that arises from the aforementioned radiative shocks.

The templates were convolved to the resolution of the longest wavelength point spread function of the IRS cube and then resampled to the same pixel grid. For the [O III] template a few additional reduction steps were necessary prior to the convolving and alignment. The processed line (F475W) and continuum (F550M) images from HST were provided to us by S. Finkelstein. The wide F475W filter was used to ensure detection of the high velocity emission from the remnant. Relative to the point sources in the image, the remnant emission is quite faint. Thus, to properly construct a template it was necessary to remove the point sources from the image by subtracting the continuum image from the line image. This was done by first cross-convolving the two images with theoretical ACS PSFs from TinyTim (Krist 1995) for the given wavebands, scaling, and subtracting. For bright point sources, the PSF subtraction often left large residuals, which were removed with a combination of median filtering and masking by hand for the bright-

TABLE 1
EMISSION LINES IN THE MID-IR SPECTRUM OF E 0102

Line	Measured Wavelength (μm)	Central Intensity (MJy sr^{-1})	Integrated Strength ($10^{-7} \text{ W m}^{-2} \text{ sr}^{-1}$)
[Ne II]	12.8053 ± 0.0005	6.287 ± 0.035	2.585 ± 0.015
[Ne III]	15.5514 ± 0.0010	2.295 ± 0.019	0.917 ± 0.022
[Ne V]	24.3460 ± 0.0053	0.566 ± 0.015	0.234 ± 0.017
[O IV]	25.9022 ± 0.0010	4.662 ± 0.019	2.132 ± 0.014

NOTE. — These measured values are from Gaussian fits to the IRS spectra.

est, saturated stars. The three templates are shown in Figure 6 after convolution and resampling to the LL pixel grid.

The decomposition at each wavelength was done with a least squares fit that constrained the coefficient of each template image to be greater than or equal to zero. The fit returns the best coefficients of the linear combination of the three templates that match the observed surface brightness distribution. Examples of the decomposition are shown in Figures 7 and 8 for two images which show $20.5 - 22.3 \mu\text{m}$ dust continuum and the [O IV] emission line at $25.9 \mu\text{m}$, respectively. To obtain the images used for these plots we have binned the cube in wavelength to increase the signal-to-noise of the image. Figure 9 shows the results of the decomposition for all wavelengths. The error bars on the plot include covariance between the three templates. One can interpret each of these results as the spectrum of the emission from the region described by each template: the x-ray emitting reverse-shocked ejecta, the [O III] emitting reverse shocked ejecta in dense knots and the forward shocked CSM/ISM material.

It is clear from the residuals shown in Figures 7 and 8 that the correspondence between the templates and the observations, while good, misses some features of the infrared emission. There is a persistently bright region in the lower left of the images which has no counterpart in the combined template. At the wavelength of strong emission lines the combined template subtraction leaves a ring of emission which most likely represents an undersubtraction of the background at these wavelengths. Because of these issues, when determining the best fit dust mass we consider the most reliable answer to be from the fit to the total remnant spectrum, rather than the combination of the spectra associated with x-ray and [O III] emitting ejecta.

Despite these uncertainties there are some strong conclusions that can be drawn from the decomposition results. One results that is a good test for the technique is that all of the line emission is found to come from the regions traced by optical [O III] emission, as expected. Other results of the decomposition are: 1) that the spectrum associated with the x-ray emitting ejecta shows dust continuum but no emission lines, 2) there is some dust continuum in the region traced by [O III] emission, which seems to peak at a wavelength around $22 \mu\text{m}$ and 3) the forward shock spectrum also has a small dust emission component that peaks around $20 \mu\text{m}$. We discuss the implications of the forward shocked dust further in Section 4.5.

3.3. Modeling the Dust Emission

3.3.1. Constructing the Dust Model

Having established that the mid-IR dust continuum emission from E 0102 mainly originates in the reverse shocked ejecta of the remnant, we now proceed to model the dust emission to attempt to place limits on the total amount of dust formed in the CCSN. Because we only see emission from material that has been reheated by the reverse shock, our model for the dust must include only the types of dust that can form out of the nucleosynthetic materials present in the layers of ejecta that are shocked (Kozasa et al. 1989; Nozawa et al. 2003). A crucial observation is that the ejecta in SNR E 0102 do not appear to be mixed. Observations at x-ray (Flanagan et al. 2004; Sasaki et al. 2001; Gaetz et al. 2000; Rasmussen et al. 2001; Hayashi et al. 1994), ultraviolet (Sasaki et al. 2006), optical (Finkelstein et al. 2006; Tuohy & Dopita 1983; Blair et al. 2000, 1989) and now infrared only detect emission from oxygen, neon, carbon, magnesium and silicon. This is in contrast to the similar O-rich remnant Cas A, which shows emission from sulfur, argon, calcium and iron as well (Hwang et al. 2004; Fesen et al. 2006; Rho et al. 2008). Either the nucleosynthetic layers of the progenitor star appear to have undergone some macroscopic mixing in Cas A or the reverse shock has encountered the oxygen-burning layers and the carbon-burning layers, for instance, in different parts of the supernova, simultaneously (Ennis et al. 2006). The same is not true of E 0102 where we see only nucleosynthetic products from the carbon-burning layers. This is most likely a consequence of the ejecta being stratified and unmixed.

Nozawa et al. (2003) model the condensation of dust in the unmixed ejecta of core-collapse supernovae. The types of dust they predict are amorphous carbon in the He-rich layers; Al_2O_3 , Mg_2SiO_4 (forsterite) and MgO in the O-Mg-Si layer; MgSiO_3 and SiO_2 in the O-Si-Mg layer; and silicon and iron rich species in the deeper nucleosynthetic layers. To construct our model for the dust in E 0102 we first consider how deeply into the ejecta the reverse shock has propagated, and thus what species of dust we should include in our model. Measurements of the abundances of oxygen, neon, magnesium and silicon in the x-ray spectra of the shocked ejecta demonstrate that magnesium is ~ 2 times more abundant than silicon (Flanagan et al. 2004). The relative amounts of these two elements locate the reverse shock in the O-Mg-Si layer. For this reason, in our dust model we assume the primary species are amorphous carbon, Al_2O_3 , forsterite and MgO as predicted for the O-Mg-Si layer and the He-rich layer by Nozawa et al. (2003).

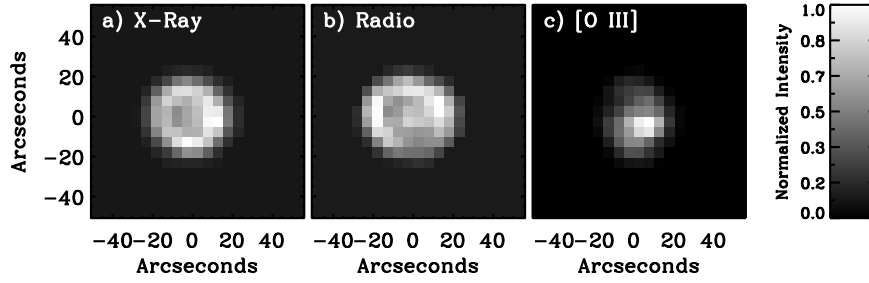


FIG. 6.— Convolved and aligned x-ray, optical and [O III] templates used in decomposing the mid-IR emission. Data are from Gaetz et al. (2000) in the x-ray, Amy & Ball (1993) in the radio and Finkelstein et al. (2006) in the optical.

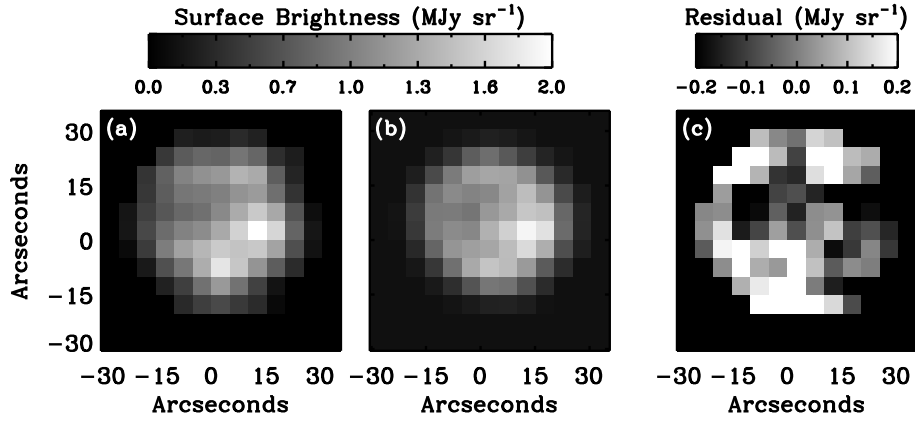


FIG. 7.— Results of the spatial decomposition for a stack of continuum images between 20.5 and 22.3 μm . We show the stacked image in order to increase the signal-to-noise ratio for display purposes. Panel a) shows the stack, Panel b) shows the best fit combination of the three templates and Panel c) shows the residuals of the fit. Note that the residual image has a different grey scale than the images in the Panels a) and b). While the linear combination of the templates reproduces most of the features of the mid-IR images, the residuals do have some persistent features.

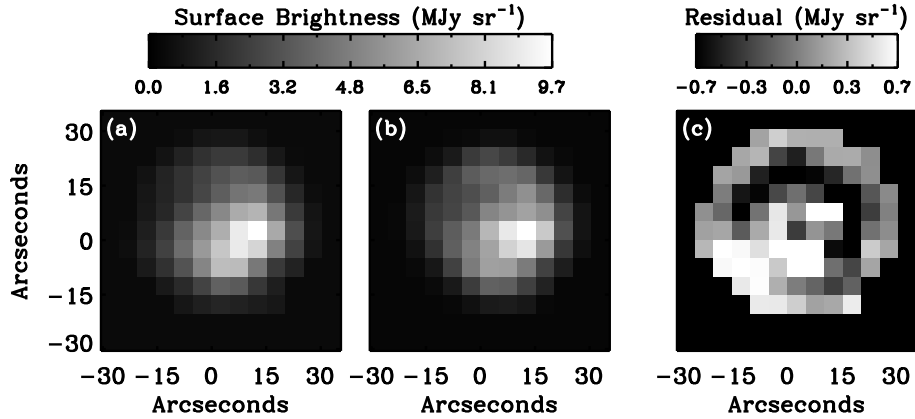


FIG. 8.— Same as in Figure 7 but for the [O IV] emission line at 25.9 μm . Note that the grey scale for the residual image has a different scale than the other images. The ring of emission visible in the residual image is most likely due to a slight undersubtraction of the background in the vicinity of a bright emission line.

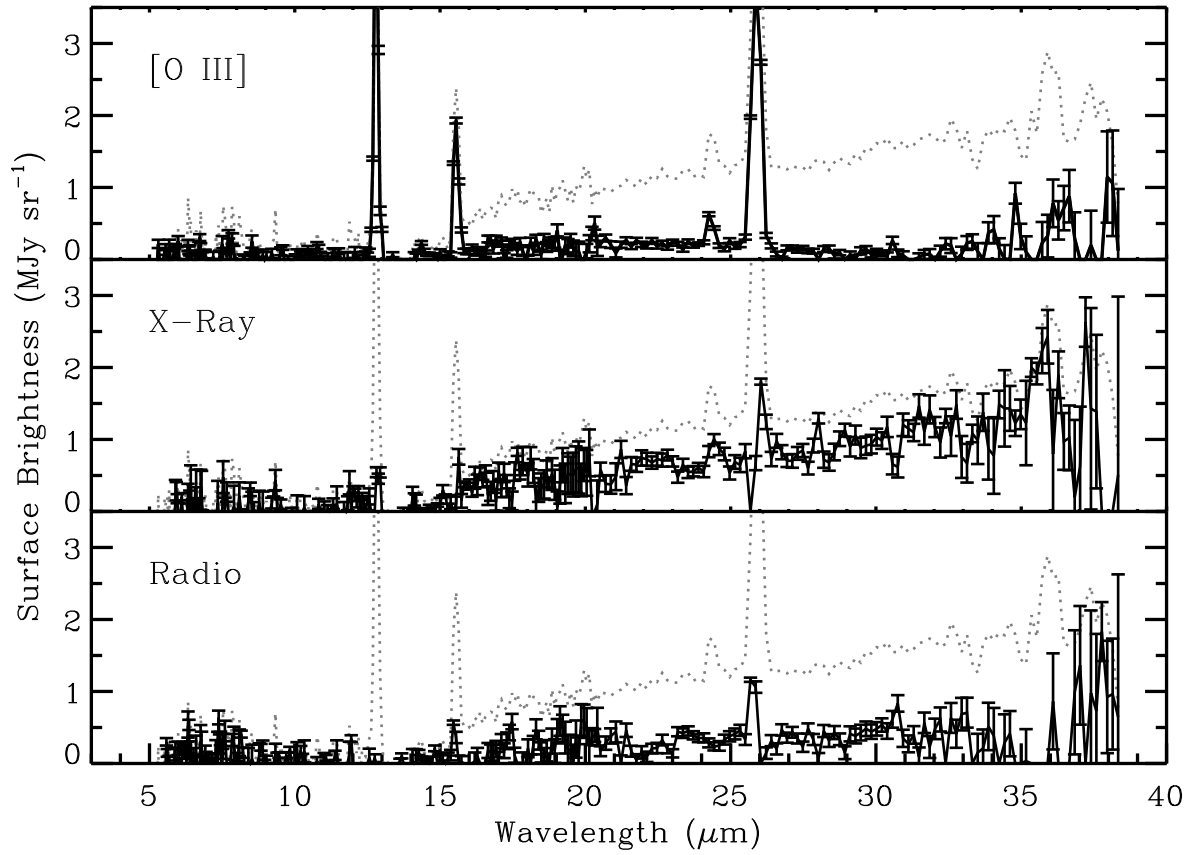


FIG. 9.— Results of the spatial decomposition of the mid-IR spectrum. Each panel shows the spectrum of the emission associated with each tracer. Error bars include the covariance between the tracers. Spikes in the x-ray and radio results in the vicinity of spectral lines are artifacts of the decomposition technique. The dotted line overplotted in each panel shows the total remnant spectrum. The [O III] template traces the emission from dense knots of reverse shocked ejecta, the x-ray template traces shocked ejecta and the radio template traces shocked CSM/ISM.

The importance of this approach to the determination of the dust mass in E 0102 arises from trying to find a physically motivated and yet unique model for the dust composition. Given enough dust species out of the complicated mineralogy of dust condensation, one could imagine any number of degenerate fits to the mid-IR spectrum. By restricting the dust model to amorphous carbon, Al_2O_3 , MgO and forsterite we hope to obtain physically meaningful values for the dust mass of each species. As we will discuss further below, even with these constraints the fit is not entirely unique, demonstrating the challenges of dealing with dust continuum emission.

3.3.2. Upper Limit at $70\mu\text{m}$

An important constraint on our determination of the dust mass from the mid-IR spectrum is the upper limit for the surface brightness of the supernova remnant at $70\mu\text{m}$ from the S^3MC MIPS observations. Contamination by the local foreground is higher at longer wavelengths because of the increasing contribution from cooler dust and the lower resolution at $70\mu\text{m}$ means it is more difficult to separate the remnant from the shoulder of N76. For these reasons determining the upper limit is not straightforward. There is no obvious emission visible from the supernova remnant in the MIPS $70\mu\text{m}$ image. To place a limit on the remnant's surface brightness we subtract a local background using the same technique outlined in Section 2.2 with a mask region $40''$ in radius to avoid contamination from the remnant, since the angular resolution at $70\mu\text{m}$ is $18''$. The background subtraction leaves emission consistent with zero, with an error of $\sim 1.0 \text{ MJy sr}^{-1}$ in the mean. We conservatively adopt a $2\text{-}\sigma$ upper limit of 2.0 MJy sr^{-1} at $70\mu\text{m}$ in the dust fitting to be conservative.

3.4. Dust Model Fit Results

We performed a non-linear least squares fit to determine the best fit dust model including the upper limit at $70\mu\text{m}$. We first fit to the total spectrum of the remnant extracted over a $22''$ radius region from the background subtracted cube. Our dust model involves the four grain species discussed above with a fixed size of $0.1\mu\text{m}$. For dust grains in the Rayleigh limit the dust mass is independent of the grain size, so fixing the size at $0.1\mu\text{m}$ does not affect the fit. The parameters of the model are the mass of dust in each species and its temperature. We also performed the fit on the total remnant spectrum minus the spectrum associated with the decomposed radio emission shown in Figure 9. The results from these two fits are very similar, as shown in Table 2. Removing the spectrum associated with the shocked CSM/ISM slightly increases the steepness of the long wavelength continuum leading to more cool dust in the fit.

The spectrum of the remnant is well fit by a combination of forsterite (Mg_2SiO_4) and amorphous carbon dust as shown in Figure 10. Neither Al_2O_3 nor MgO play an important role in the best fit model. Upper limits on the masses of Al_2O_3 and MgO are listed in Table 2 at a temperature of 70 K. At higher temperatures the limits on the masses are stricter. The best fit forsterite component has a temperature of 145 K while the amorphous carbon component, which contains most of the dust mass we detect, has a temperature of 70 K.

However, the fit results for the cool dust component are not unique. A fit of similar quality using two temperature components of forsterite is listed in Table 2 as well. The continuum shape around $20\mu\text{m}$ is not well reproduced without forsterite in the dust model, however the longer wavelength continuum shape does not distinguish strongly between forsterite and amorphous carbon. In the following we proceed by assuming that the dust is amorphous carbon because 1) it provides a more conservative estimate of the dust mass (i.e. a lower limit) and 2) theoretical predictions suggest that there should be a substantial amount of amorphous carbon which, if present, should all be in the reverse shocked outer layers and visible to us in the mid-IR.

The $70\mu\text{m}$ upper limit does not affect the amount of forsterite we measure. On the other hand, the limit does affect both the mass and temperature of the amorphous carbon dust. Decreasing the limit tends to make the amorphous carbon dust warmer and less massive, increasing it makes the amorphous carbon cooler and more massive. We note that for limits below about 1 MJy sr^{-1} the fit no longer converges properly, because the limit is inconsistent with the slope of the data past $30\mu\text{m}$. We predict that with a small increase in signal-to-noise and/or angular resolution the remnant should be detectable at $70\mu\text{m}$.

We also perform individual fits to the spectra associated with the x-ray, [O III] and radio templates in order to learn about the dust in the x-ray emitting reverse shocked ejecta, the dense knots of reverse shocked ejecta and the CSM/ISM dust in the forward shock. Figure 11 shows the dust continuum associated with the radio and [O III] templates and the fit listed in Table 2. The continuum shape and signal-to-noise in the spectrum associated with the radio template do not strongly constrain the species of dust present in the CSM/ISM material. We show a representative fit with interstellar graphite from Laor & Draine (1993). The fits imply $\sim 10^{-6} - 10^{-5} M_\odot$ of dust with a temperature around 150 – 180 K. We discuss this component further in Section 4.5. The dust continuum associated with the [O III] emitting knots has a better defined shape that is well reproduced by forsterite but not amorphous carbon. Fits to that component yield a dust mass of $\sim 2 \times 10^{-6} M_\odot$ of forsterite at 180 K.

Using a simplified version of the model which involves only forsterite and amorphous carbon, we performed the fit at each pixel in the map in order to learn about the spatial distribution of the dust species. These results are shown in Figures 12 and 13. The forsterite to amorphous carbon ratio tracks the intensity of the x-ray ring of the reverse shock. This resemblance may be an indication that forsterite is more abundant in the deeper layers of the ejecta which are now encountering the reverse shock.

4. DISCUSSION

4.1. Newly Formed Dust

We detect $3 \times 10^{-3} M_\odot$ of 70 K amorphous carbon and $2 \times 10^{-5} M_\odot$ of 145 K forsterite in the ejecta of E 0102. The equilibrium temperatures of grains in the x-ray emitting plasma are between 50 and 100 K for sizes between 1.0 and $0.001\mu\text{m}$. The temperature we measure for the amorphous carbon component corresponds to the equilibrium temperature for grains with sizes of ~ 0.1

TABLE 2
FIT RESULTS

Spectrum	Model	Mass (M_{\odot})	Temperature (K)
Total Spectrum	Al_2O_3	$< 1 \times 10^{-6}$	> 70
	Am. Carbon	3×10^{-3}	70
	MgO	$< 1 \times 10^{-5}$	> 70
	Mg_2SiO_4	2×10^{-5}	145
Total Spectrum	Mg_2SiO_4	2×10^{-5}	145
	Mg_2SiO_4	1×10^{-2}	54
Total Spectrum – CSM/ISM	Am. Carbon	6×10^{-3}	60
	Mg_2SiO_4	2×10^{-5}	145
X-ray Emitting Reverse Shocked Ejecta	Am. Carbon	4×10^{-3}	60
	Mg_2SiO_4	8×10^{-6}	150
[O III] Emitting Reverse Shocked Ejecta	Mg_2SiO_4	2×10^{-6}	180
CSM/ISM	ISM Graphite	8×10^{-6}	170

NOTE. — Optical constants for amorphous carbon from Rouleau & Martin (1991) and ISM graphite from Laor & Draine (1993). The sources for the other optical constants can be found in Table 3.

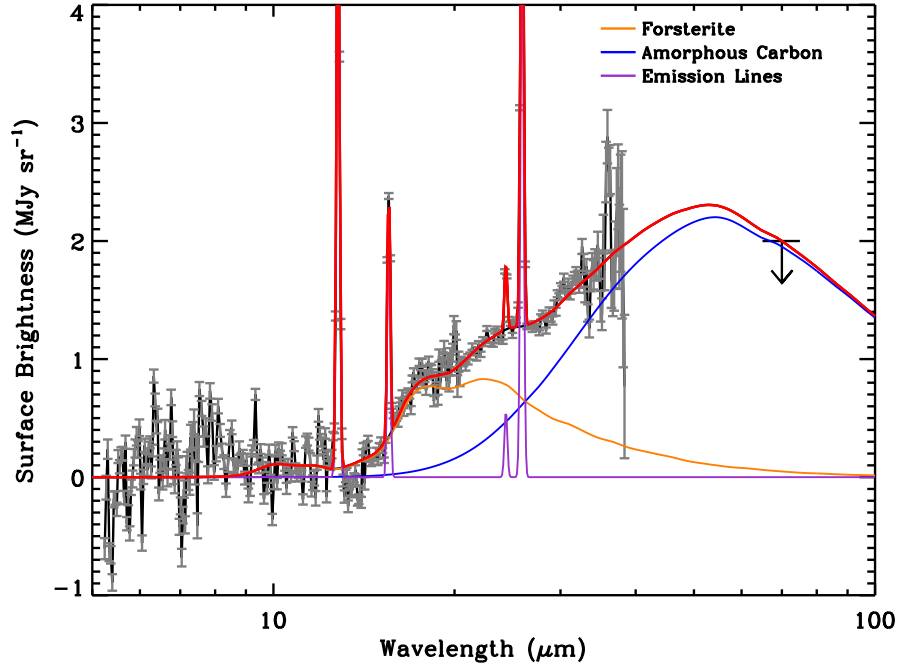


FIG. 10.— Dust model fit to the spectrum showing $3 \times 10^{-3} M_{\odot}$ of 70 K amorphous carbon and $2 \times 10^{-5} M_{\odot}$ of 145 K forsterite. The 145 K forsterite component is necessary to reproduce the continuum shape below $\sim 30 \mu\text{m}$. The 60 K dust component is less constrained and could be replaced with forsterite at a comparable temperature with no impact on the quality of the fit. The arrow shows the upper limit at $70 \mu\text{m}$.

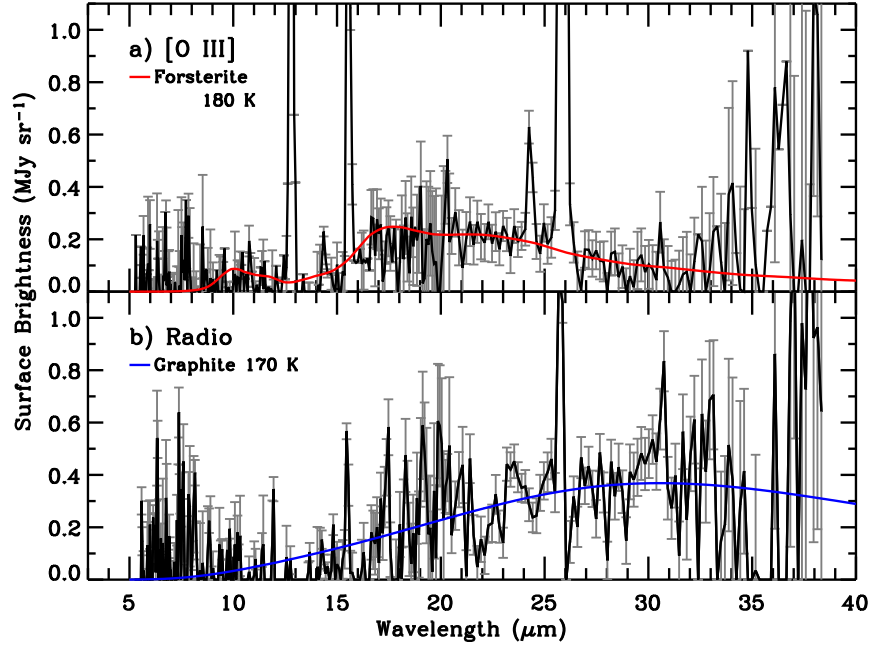


FIG. 11.— This figure shows a zoomed in version of the spectra associated with the [O III] and radio templates from the spatial decomposition along with a fit to the dust continuum. The fit to the spectrum associated with the radio template is representative. Since we expect it to be interstellar dust we have used interstellar graphite from Laor & Draine (1993). Silicate also reproduces the continuum shape at the same level of quality. For the [O III] knots, however, the shape of the continuum is not well reproduced by amorphous carbon. The fit using forsterite is quite good, given the uncertainties involved.

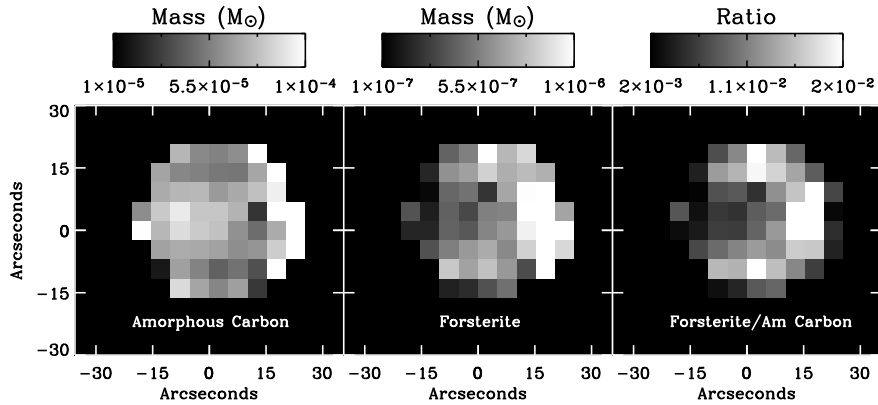


FIG. 12.— Dust masses determined at each pixel. The first panel shows the mass of amorphous carbon, the second shows the mass of forsterite and the third shows the ratio of forsterite to amorphous carbon. The ratio is highest at the boundary of the reverse shock which agrees with the idea that the reverse shock is just beginning to encounter the O-Mg-Si layer where forsterite has been produced.

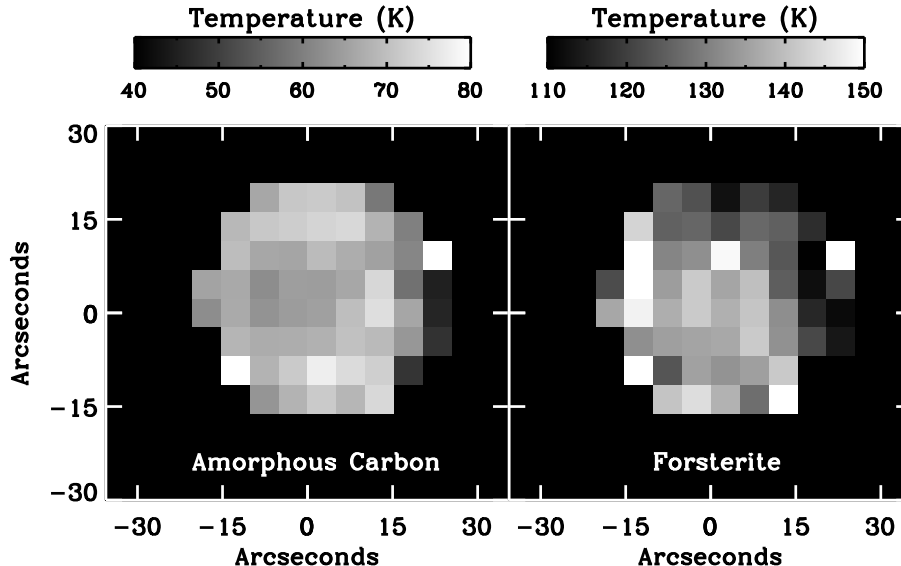


FIG. 13.— Dust temperatures determined at each pixel. The temperature of the amorphous carbon dust is consistent with grains of $\sim 0.1 \mu\text{m}$ in equilibrium with the x-ray emitting reverse-shocked plasma. The forsterite component has temperatures which are higher than the predicted equilibrium in the x-ray emitting plasma. This may be the result of the forsterite abundance increasing deeper in the ejecta, as suggested by the forsterite to amorphous carbon abundance shown in Figure 12, where the recent passage of the reverse shock has not yet destroyed smaller grains which can be stochastically heated.

μm . Figure 5 verifies that grains of this size should be in equilibrium.

The temperature of the forsterite dust component is hotter than the equilibrium temperature that could be achieved by grains in the x-ray emitting plasma of the reverse shock, but is consistent with temperatures in the dense [O III] emitting knots. In fitting the decomposed spectrum associated with the [O III] emission we do see forsterite with temperatures around 180 K, typical for grains with sizes around $0.01 \mu\text{m}$ under the expected conditions. If, however, most of the forsterite is located in the x-ray emitting plasma, as the results of our spatial decomposition suggest, the temperature would imply small dust grains that are stochastically heated. In the following section we show that the sputtering timescale in the reverse shocked ejecta for small grains is less than the age of the remnant. The presence of small, stochastically heated dust grains in the x-ray emitting plasma can be explained if the dust has only recently been through the reverse shock, such that it has been in the plasma for less than the sputtering time. Given the results shown in Figure 12, i.e. that the abundance of forsterite seems to increase near the bright, inner boundary of the reverse shock, this may very well be the explanation for why we see forsterite grains out of equilibrium with the plasma.

4.2. Dust Sputtering and Grain Size Constraints

The dust we see in E 0102 at present may not be the amount that was initially produced in the supernova or what was initially swept up by the blast wave. Dust grains in shock waves can be destroyed by sputtering, where impacts by hot gas particles erode the grain.

For the dust in the forward shocked ISM/CSM we can estimate the sputtering time with the relation

$$\tau_{sp} \sim \frac{a}{da/dt} \sim 10^6 \frac{a}{\mu\text{m}} \left(\frac{n_e}{\text{cm}^{-3}} \right)^{-1} \text{yr}, \quad (4)$$

from Draine & Salpeter (1979) for gas with temperatures greater than $\sim 10^6 \text{ K}$ and solar abundances. In this regime the majority of the sputtering is done by hydrogen ions and $n_e \approx n_H$, so the abundance of heavier elements does not significantly affect the calculations and we can use these results for the SMC metallicity. Following the discussion in Section 3.1.1, we estimate densities in the x-ray emitting forward shocked material of $\sim 1 \text{ cm}^{-3}$. Thus, the sputtering timescale for dust grains in the forward shock is $\sim 10^5$ years for an $0.1 \mu\text{m}$ grain and $\sim 10^3$ years for an $0.001 \mu\text{m}$ grain. Given the age of the remnant, dust grains with sizes below $0.001 \mu\text{m}$ should have been destroyed behind the shock.

In the reverse shocked gas the sputtering of dust is due to collisions with oxygen ions, since oxygen is the dominant component of the ejecta. We can use a simple scaling argument based on the sputtering time relation above to estimate the lifetime of grains in the reverse shocked material. The sputtering rate R in (g s^{-1}) is given by

$$R \sim \sigma n v Y, \quad (5)$$

where n and v are the density and velocity of the sputtering particles, σ is the grain cross section and Y is the sputtering yield per collision in units of mass per collision. Therefore, the change of grain radius with time, assuming constant density for the grain and a thermal velocity for the colliding particles $v \sim (kT/m)^{1/2}$, goes as:

$$\frac{da}{dt} \propto n T^{1/2} m^{-1/2} Y. \quad (6)$$

Scaling the sputtering between the forward shock and reverse shock gas involves a number of assumptions. First, the density of oxygen ions in the reverse shock is not simply related to the electron density, because the ionization state of the gas is not in equilibrium (in which case the number of free electrons donated per oxygen

atom would be a predictable function of the temperature). Second, the temperature of the oxygen ions is not an easily determined quantity either, given the uncertain equilibration timescale between the electrons and the ions after the shock. As an estimate we can assume $n_{\text{O}} \sim n_e/3$ as a reasonable value for the number of free electrons donated by each oxygen atom, and $T_{\text{O}} \sim T_e$, which should be the case if the equilibration timescale between the ions and electrons is less than ~ 1000 years. In the case where the ions are hotter than the electrons, the sputtering timescale will decrease. Nozawa et al. (2007) investigated the sputtering of dust grains in the reverse shocks of supernova remnants and via fits to experimental data for a variety of grain compositions and collider properties found that sputtering by oxygen ions has ~ 50 times higher yield than sputtering by hydrogen ions. Using these values ($n_{\text{O}} \sim n_e/3$, $T_e \sim T_{\text{O}}$, and $Y_{\text{O}} \sim 50Y_{\text{H}}$) we estimate that the sputtering timescale in the reverse shocked ejecta, which has an electron density of $\sim 20 \text{ cm}^{-3}$, for a grain of size $0.1 \text{ } \mu\text{m}$ is ~ 1000 years. Thus, in the x-ray emitting, oxygen-rich ejecta, the destruction time for grains smaller than $0.1 \text{ } \mu\text{m}$ is shorter than the age of the remnant and we expect that the grain size distribution in the plasma has been altered significantly.

The amorphous carbon dust, which makes up the majority of the mass we detect from the reverse shocked ejecta, has a temperature which suggests emission from $\sim 0.1 \text{ } \mu\text{m}$ grains. Based on our estimate of the sputtering timescale in the reverse shocked plasma, these grains would be able to survive the lifetime of the remnant. The warmer forsterite dust component is found to be associated with the dense [O III] knots, which have a higher equilibrium temperature due to their high densities, and with the most recently reverse-shocked ejecta, in which smaller dust grains may still exist and be stochastically heated to higher temperatures.

4.3. The Possibility of Cold Dust

Because our observations are only sensitive to warm, recently shocked dust, we cannot quantify the total amount of newly formed dust produced in the remnant. To understand the limits that the $70 \text{ } \mu\text{m}$ observation places on the mass of cold dust, we construct a model for the unshocked dust in the supernova remnant based on the condensation models of Nozawa et al. (2003) for a $25 M_{\odot}$ progenitor. We list the dust species included in the model, the source for their optical constants, and the masses predicted by Nozawa et al. (2003) in Table 3. The total mass of dust predicted by their models is $0.6 M_{\odot}$, minus the amorphous carbon component which we argue must primarily be in the outer, shocked layers of the ejecta. In Figure 14 we show the remnant’s spectrum, the best fit model with amorphous carbon and forsterite from Section 3.4, and the spectrum of the cold dust at temperatures of 20 (blue) and 35 K (black). It is clear that our limit at $70 \text{ } \mu\text{m}$ does not preclude the possibility of a substantial mass of cold dust in the remnant, since at a temperature of 20 K, the entire predicted mass of dust can be hidden at $70 \text{ } \mu\text{m}$. Determining the total amount of newly formed dust in E 0102 will require longer wavelength observations.

4.4. Implications for Dust Production in CCSN and Comparison with Previous Results

Stanimirović et al. (2005) found a mass of $8 \times 10^{-4} M_{\odot}$ of dust in E 0102 based on the flux at $24 \text{ } \mu\text{m}$. Using upper limits at 8 and $70 \text{ } \mu\text{m}$, they argued that the dust had to have a temperature around 120 K. They assumed that 60% of the $24 \text{ } \mu\text{m}$ emission was from the contribution of [O IV], a value we measure to be 15%. These differences alone do not explain the ~ 4 times more dust that we find compared to Stanimirović et al. (2005). Instead, the greater contribution of cooler dust with a temperature of around 70 K accounts for most of the difference. Our measurement of the temperature and mass of forsterite dust are comparable to their predictions. The spectrum past $30 \text{ } \mu\text{m}$, however, is not compatible with only a ~ 120 K component.

Similar mid-infrared spectral mapping observations have been carried out on Cas A, another young, oxygen-rich CCSN remnant, by Rho et al. (2008). There are some important differences between the observations. Cas A’s relative proximity and brightness allows more detailed fits to the spectrum of the remnant. Cas A also has emission from S, Si, and Ar in its spectrum in addition to O, Ne, and Mg. This could be the result of macroscopic mixing, as suggested by Douvion et al. (1999), or of velocity inhomogeneity (Smith et al., in prep.), causing different layers of the ejecta to encounter the reverse shock simultaneously. In both of these situations, the overall composition of the nucleosynthetic layers is preserved and the same species of dust should have formed in the ejecta as in E 0102. It may not be possible, however, to separate different nucleosynthetic layers spatially, making the modeling more complex.

Rho et al. (2008) find on the order of $0.02 - 0.05 M_{\odot}$ of dust in the Cas A remnant, with contributions from a variety of dust species. They find three distinct spectra in Cas A, a $21 \text{ } \mu\text{m}$ peak spectrum, a weak $21 \text{ } \mu\text{m}$ spectrum and a featureless spectrum. The weak $21 \text{ } \mu\text{m}$ spectrum has associated strong neon lines, similar to what we see in E 0102. The dominant dust components by mass that Rho et al. (2008) fit to the weak $21 \text{ } \mu\text{m}$ spectrum are two temperature components of amorphous carbon at ~ 80 and ~ 200 K totaling $\sim 1 - 2 \times 10^{-3} M_{\odot}$ and $\sim 0.6 - 1.4 \times 10^{-2} M_{\odot}$ of FeO at ~ 60 K. The mass of amorphous carbon we find is comparable to their results, however we have no evidence of FeO in our spectrum and it seems unlikely that a substantial amount of FeO could be produced, since it requires microscopic mixing of the ejecta. Comparing with the total amount of dust that Rho et al. (2008) find in Cas A, we see similar amounts of both amorphous carbon and Mg_2SiO_4 , on the order of 10^{-3} and $10^{-5} M_{\odot}$ respectively. However, they argue for significant amounts of Fe, FeO, FeS and SiO_2 , producing a total dust mass of between $0.02 - 0.05 M_{\odot}$ of newly-formed dust—an order-of-magnitude larger than what we observe in E 0102. The progress of the reverse shock into the deeper nucleosynthetic layers of Cas A may partially account for the difference in the observed dust mass between the two remnants. It is possible that similar dust masses could be present but the iron- and silicon-rich dust species are in unshocked layers of the ejecta of E 0102 and are too cold for us to detect in these observations.

Given the progress of the reverse shock into the ejecta, we can claim with good confidence that we should see essentially all of the amorphous carbon dust that has been

TABLE 3
COLD DUST MODEL COMPONENTS

Species	Mass (M_{\odot})	Optical Constants	Reference
Mg ₂ SiO ₄	0.2	Jäger et al. (2003)	
Amorphous Silicon	0.2	Piller (1985)	
SiO ₂	0.07	Philipp (1985)	
FeS	0.07	Begemann et al. (1994)	
MgO	0.06	Roessler & Huffman (1991)	
Fe	0.02	Lynch & Hunter (1991)	
MgSiO ₃	0.003	Dorschner et al. (1995)	
Al ₂ O ₃	0.002	Begemann et al. (1997)	

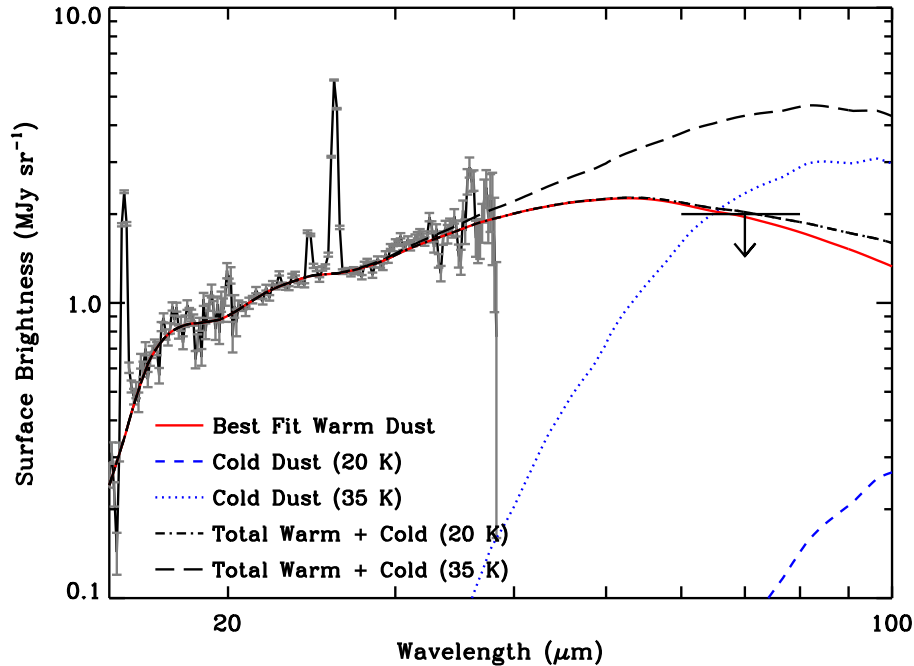


FIG. 14.— This figure shows predictions for the far-IR spectrum of dust in the remnant using the cold dust model components listed in Table 3. The cold dust spectrum contains the total dust mass predicted by the Nozawa et al. (2003) models for a $25 M_{\odot}$ progenitor excluding amorphous carbon. The dashed line shows this model assuming the cold dust has a temperature of 20 K and the dotted line shows the same model with a temperature of 35 K. The black dash-dot and long-dashed lines show the total spectrum of cold dust plus the warm dust we detect in the mid-IR. This plot demonstrates that all of the predicted $\sim 0.6 M_{\odot}$ of dust can be present in the remnant if it has a temperature of 20 K, showing that our current observations alone can not strongly constrain the dust condensation efficiency.

produced in the mid-IR. This being the case, we find substantially less amorphous carbon dust than predicted by dust condensation models. The models of Nozawa et al. (2003) predict on the order of $10^{-1} - 10^{-2} M_{\odot}$ of amorphous carbon, whereas we only see $\sim 3 \times 10^{-3} M_{\odot}$. We estimate that the sputtering time for dust in the reverse-shocked ejecta is less than the age of the remnant, so we may be observing less dust than was initially formed. Nozawa et al. (2007) calculate the dust destruction via sputtering in the reverse shock for the same models quoted above using a simple prescription for the interaction of the ejecta with the surrounding ISM. They find that for an ambient density of 0.1 cm^{-3} , only 8% of the amorphous carbon dust is destroyed for their $25 M_{\odot}$ progenitor. Most of the mass of carbon dust in that model is in grains with sizes greater than $0.05 \mu\text{m}$, which have longer sputtering lifetimes. We have no constraints on the initial grain size, so it is difficult to estimate how

much of the dust in the remnant has been destroyed up to this point.

Previous observations of newly formed dust in CCSN have yielded dust masses in the range of 10^{-3} to $10^{-5} M_{\odot}$, with some controversial measurements claiming higher masses. The majority of the measurements come from CCSN of Type II or their remnants, which have hydrogen envelopes and red supergiant progenitors. Dust formation has been observed in two Type Ib events: SN 1990I (Elmhamdi et al. 2004) and the peculiar event SN 2006jc (Smith et al. 2008; Nozawa et al. 2008) which shows evidence for dust formation at very early times, around 50 days after the explosion. The masses determined from observations of 2006jc range from a few 10^{-6} to a few 10^{-3} depending on the observation date, wavelength and dust model. Recently, Nozawa et al. (2008) have modeled dust condensation in a Type Ib event in order to assess the effects of a small or non-existent hy-

drogen envelope on the dust condensation efficiency. The high expansion velocities mean that the density drops quickly, leading to dust condensation at earlier times in these events. The condensation efficiency is high, however, yielding $0.7 M_{\odot}$ of amorphous carbon in their model of SN 2006jc, which is in contrast to the relatively small amount of dust detected in the near-IR and mid-IR observations. Our results for E 0102 lie near the upper bounds of the observed dust mass in SN 2006jc. It may not be the case, however, that dust is forming in the ejecta of SN 2006jc. Smith et al. (2008) argue that the dust condensation occurs in the cooling region of the shocks created by the interaction of the blast wave with an expanding shell of circumstellar material. If this is the case, we may not expect to see comparable species or amounts of dust in SN 2006jc and E 0102.

4.5. The Circumstellar Environment of SNR E 0102

The progenitor of SNR E 0102 was most likely a massive star that lost most of its hydrogen/helium envelope before exploding as a Type Ib/Ic or IIb/L supernova (Blair et al. 2000; Chevalier 2005). As such, it would have significantly impacted the circumstellar medium in the form of winds and mass loss. Here we briefly discuss what we can learn about the CSM/ISM from our observations.

The spectrum associated with the radio continuum template, as discussed in Section 3.2, shows the dust continuum emission from forward shocked CSM/ISM material. Fits to this spectrum with interstellar graphite and silicate grains give masses in the range $10^{-5} - 10^{-6} M_{\odot}$ and temperatures of ~ 180 K. If the remnant were expanding into the average SMC interstellar medium with a density of $n \sim 0.1 \text{ cm}^{-3}$, we would expect approximately $2 M_{\odot}$ of swept up gas and $\sim 3 \times 10^{-3} M_{\odot}$ of swept up dust at this point in time (using a dust to gas ratio of 1/700 as determined by Leroy et al. 2007). Although the fit dust mass is far less than this expected value, the temperature indicates that the dust we see is not in collisional equilibrium and therefore we are only detecting the fraction of the dust that is warm at a given time (see Figure 4 for the predicted equilibrium temperature in the forward shock).

For stochastic heating, the fraction of grains which are warm at any time is given approximately by the ratio of the collision time to the cooling time $f \sim \tau_{\text{cool}}/\tau_{\text{coll}}$. This ratio is shown as a function of grain size in Figure 5. Grains with $a > 0.02 \mu\text{m}$ will not be stochastically heated and will have equilibrium temperatures between 40 and 70 K. In Section 4.2, we estimated that grains with $a < 0.001 \mu\text{m}$ should be destroyed by sputtering on timescales shorter than the age of the remnant. Within these limits $0.001 < a < 0.02$, we can estimate that $f \sim 0.01 - 1$, i.e. that we detect between 1 and 100% of the dust mass in the forward shocked CSM/ISM. Thus, the amount of dust in the forward shocked CSM/ISM is essentially unconstrained by our observations, ranging from $10^{-6} - 10^{-3} M_{\odot}$.

Depending on the progenitor star and its winds, we may not expect to see any dust in the forward-shocked plasma. This would be the case if the blast wave has not yet reached the pristine ISM and the circumstellar medium has been cleared of dust by the winds of the progenitor star. Chevalier (2005) argue that E 0102 is still

interacting with the wind of its progenitor star based on the positions of the forward and reverse shocks and the lack of limb brightening in the x-ray emission from the forward shock. The dust content of the circumstellar medium will depend on the duration of the wind and the previous evolution of the progenitor (for example, whether there were outbursts similar to those observed from the progenitor of SN 2006jc (Pastorello et al. 2007)) among other factors. Further observational constraints on the progenitor mass and evolution will be necessary to understand whether the dust we see associated with the forward shock fits with the overall picture of the evolution of E 0102.

5. SUMMARY & CONCLUSIONS

To summarize, we present mid-IR spectral mapping observations of the supernova remnant 1E 0102.2–7219 in the vicinity of N 76 in the Small Magellanic Cloud. The ~ 1000 year old, oxygen-rich remnant is thought to be the product of a Type Ib/Ic or IIb/L supernova. Currently the reverse shock, produced by the dynamical interaction of the ejecta with the surrounding ISM/CSM, is propagating back through the ejecta. Based on spectroscopic observations at x-ray, ultraviolet, optical and now infrared wavelengths, the ejecta down to the depth of the reverse shock appear to be composed of oxygen, neon, magnesium, silicon and carbon. This composition indicates that the reverse shock has only penetrated into the deeper layers of nucleosynthetic products and that no large-scale mixing of deeper layers has occurred.

The mid-IR spectrum of the remnant shows fine-structure emission lines of oxygen and neon on top of emission from warm dust. We use observations of the remnant at x-ray, radio and optical wavelengths as templates to decompose the infrared emission into components associated with the newly-formed dust in the reverse shocked ejecta and ISM/CSM dust in the forward shocked region. Our decomposition of the spectrum shows (1) dust continuum associated with the x-ray emitting reverse shocked ejecta, (2) oxygen and neon fine-structure emission lines and warm dust continuum associated with the optical [O III] emitting gas in dense knots of ejecta where the reverse shock is slow and radiative and (3) a small amount of dust emission associated with the forward shock. The majority of the dust is associated with the x-ray emitting reverse shocked material.

We construct a model for the newly-formed dust in the unmixed ejecta. Using x-ray measurements of the abundance of magnesium and silicon we estimate the location of the reverse shock to be in the O-Mg-Si layer. We model the dust emission with amorphous carbon, forsterite (Mg_2SiO_4), Al_2O_3 , and MgO as appropriate for the composition of the ejecta down to the depth of the O-Mg-Si layer, motivated by the results of dust condensation models. The best fit model contains $3 \times 10^{-3} M_{\odot}$ of amorphous carbon at a temperature of 70 K and $2 \times 10^{-5} M_{\odot}$ of forsterite with temperature of 145 K. The masses of Al_2O_3 and MgO are limited to be less than 1×10^{-6} and $1 \times 10^{-5} M_{\odot}$ at a temperature of 70 K, respectively, since they do not contribute substantially to the continuum shape in the mid-IR. The temperature of amorphous carbon agrees with expectations for $0.1 \mu\text{m}$ grains in the x-ray emitting plasma behind the reverse shock, which agrees with our estimate that smaller grains

have been destroyed by sputtering. The temperature of the forsterite component suggests that the emission is from smaller, stochastically heated grains which have recently been heated by the passage of the reverse shock or are residing in dense knots of ejecta material.

If the reverse shock is presently encountering material from the O-Mg-Si layer of the progenitor we should be detecting the majority of the newly-formed amorphous carbon dust, since it forms primarily in the outermost layers of the ejecta. Comparison with the Nozawa et al. (2003) results show substantially less amorphous carbon dust in E 0102 than would be predicted based on the progenitor mass. Our results for the masses of amorphous carbon and forsterite are comparable to work on Cas A by Rho et al. (2008).

Our mid-IR observations are not sensitive to cold dust present in the remnant. We show that if the dust has a temperature of 20 K, $\sim 0.6 M_{\odot}$ of dust could be present in the remnant and undetectable in our observations. Observations at longer wavelengths by Herschel, LABOCA on APEX or ALMA will be necessary to determine the amount of cold dust present in the remnant.

Without a substantial mass of hidden cold dust, the dust production in E 0102 falls orders of magnitude below what would be necessary to explain the observations of dust around high redshift quasars.

The authors would like to thank S. Finkelstein for providing us with the [O III] map. K.S. would like to thank Eli Dwek, Maryam Modjaz, and Nathan Smith for useful conversations and Adam Leroy for providing a quiet place to work at a crucial time. K.S. acknowledges the support of an NSF Graduate Research Fellowship. This work is based on observations made with the Spitzer Space Telescope, which is operated by the Jet Propulsion Laboratory, California Institute of Technology under a contract with NASA. This research was supported in part by NASA through awards issued by JPL/Caltech (NASA-JPL Spitzer grant 1264151 awarded to Cycle 1 project 3316, and grants 1287693 and 1289519 awarded to Cycle 3 project 30491).

Facilities: Spitzer ()

REFERENCES

- Amy, S. W. & Ball, L. 1993, *ApJ*, 411, 761
 Arendt, R. G., Dwek, E., & Leisawitz, D. 1992, *ApJ*, 400, 562
 Arendt, R. G., Dwek, E., & Moseley, S. H. 1999, *ApJ*, 521, 234
 Beelen, A., Cox, P., Benford, D. J., Dowell, C. D., Kovács, A., Bertoldi, F., Omont, A., & Carilli, C. L. 2006, *ApJ*, 642, 694
 Begemann, B., Dorschner, J., Henning, T., Mutschke, H., Güertler, J., Kömpe, C., & Nuss, R. 1997, *ApJ*, 476, 199
 Begemann, B., Dorschner, J., Henning, T., Mutschke, H., & Thamm, E. 1994, *ApJ*, 423, L71
 Bertoldi, F., Carilli, C. L., Cox, P., Fan, X., Strauss, M. A., Beelen, A., Omont, A., & Zylka, R. 2003, *A&A*, 406, L55
 Blair, W. P., Ghavamian, P., Long, K. S., Williams, B. J., Borkowski, K. J., Reynolds, S. P., & Sankrit, R. 2007, *ApJ*, 662, 998
 Blair, W. P., Morse, J. A., Raymond, J. C., Kirshner, R. P., Hughes, J. P., Dopita, M. A., Sutherland, R. S., Long, K. S., & Winkler, P. F. 2000, *ApJ*, 537, 667
 Blair, W. P., Raymond, J. C., Danziger, J., & Matteucci, F. 1989, *ApJ*, 338, 812
 Bode, M. F. & Evans, A. 1980, *MNRAS*, 193, 21P
 Bolatto, A. D., Simon, J. D., Stanimirović, S., van Loon, J. T., Shah, R. Y., Venn, K., Leroy, A. K., Sandstrom, K., Jackson, J. M., Israel, F. P., Li, A., Staveley-Smith, L., Bot, C., Boulanger, F., & Rubio, M. 2007, *ApJ*, 655, 212
 Bot, C., Boulanger, F., Lagache, G., Cambrésy, L., & Egret, D. 2004, *A&A*, 423, 567
 Bouchet, P., Dwek, E., Danziger, J., Arendt, R. G., De Buizer, I. J. M., Park, S., Suntzeff, N. B., Kirshner, R. P., & Challis, P. 2006, *ApJ*, 650, 212
 Chevalier, R. A. 2005, *ApJ*, 619, 839
 Dorschner, J., Begemann, B., Henning, T., Jäger, C., & Mutschke, H. 1995, *A&A*, 300, 503
 Douvion, T., Lagage, P. O., & Cesarsky, C. J. 1999, *A&A*, 352, L111
 Draine, B. T. & Anderson, N. 1985, *ApJ*, 292, 494
 Draine, B. T. & Salpeter, E. E. 1979, *ApJ*, 231, 77
 Dunne, L., Eales, S., Ivison, R., Morgan, H., & Edmunds, M. 2003, *Nature*, 424, 285
 Dwek, E. 1983, *ApJ*, 274, 175
 —. 1986, *ApJ*, 302, 363
 —. 1987, *ApJ*, 322, 812
 Dwek, E., Galliano, F., & Jones, A. P. 2007, *ApJ*, 662, 927
 Dwek, E. & Werner, M. W. 1981, *ApJ*, 248, 138
 Elmhamdi, A., Danziger, I. J., Cappellaro, E., Della Valle, M., Gouffes, C., Phillips, M. M., & Turatto, M. 2004, *A&A*, 426, 963
 Ennis, J. A., Rudnick, L., Reach, W. T., Smith, J. D., Rho, J., DeLaney, T., Gomez, H., & Kozasa, T. 2006, *ApJ*, 652, 376
 Ercolano, B., Barlow, M. J., & Sugerman, B. E. K. 2007, *MNRAS*, 375, 753
 Fesen, R. A., Hammell, M. C., Morse, J., Chevalier, R. A., Borkowski, K. J., Dopita, M. A., Gerardy, C. L., Lawrence, S. S., Raymond, J. C., & van den Bergh, S. 2006, *ApJ*, 636, 859
 Finkelstein, S. L., Morse, J. A., Green, J. C., Linsky, J. L., Shull, J. M., Snow, T. P., Stocke, J. T., Brownsberger, K. R., Ebbets, D. C., Wilkinson, E., Heap, S. R., Leitherer, C., Savage, B. D., Siegmund, O. H., & Stern, A. 2006, *ApJ*, 641, 919
 Flanagan, K. A., Canizares, C. R., Dewey, D., Houck, J. C., Fredericks, A. C., Schattenburg, M. L., Markert, T. H., & Davis, D. S. 2004, *ApJ*, 605, 230
 Gaetz, T. J., Butt, Y. M., Edgar, R. J., Eriksen, K. A., Plucinsky, P. P., Schlegel, E. M., & Smith, R. K. 2000, *ApJ*, 534, L47
 Hayashi, I., Koyama, K., Ozaki, M., Miyata, E., Tsumeni, H., Hughes, J. P., & Petre, R. 1994, *PASJ*, 46, L121
 Hirashita, H., Nozawa, T., Kozasa, T., Ishii, T. T., & Takeuchi, T. T. 2005, *MNRAS*, 357, 1077
 Hughes, J. P., Rakowski, C. E., & Decourchelle, A. 2000, *ApJ*, 543, L61
 Hwang, U., Laming, J. M., Badenes, C., Berendse, F., Blondin, J., Cioffi, D., DeLaney, T., Dewey, D., Fesen, R., Flanagan, K. A., Fryer, C. L., Ghavamian, P., Hughes, J. P., Morse, J. A., Plucinsky, P. P., Petre, R., Pohl, M., Rudnick, L., Sankrit, R., Slane, P. O., Smith, R. K., Vink, J., & Warren, J. S. 2004, *ApJ*, 615, L117
 Jäger, C., Dorschner, J., Mutschke, H., Posch, T., & Henning, T. 2003, *A&A*, 408, 193
 Kozasa, T., Hasegawa, H., & Nomoto, K. 1989, *ApJ*, 344, 325
 Krause, O., Birkmann, S. M., Rieke, G. H., Lemke, D., Klaas, U., Hines, D. C., & Gordon, K. D. 2004, *Nature*, 432, 596
 Krist, J. 1995, in *Astronomical Society of the Pacific Conference Series*, Vol. 77, *Astronomical Data Analysis Software and Systems IV*, ed. R. A. Shaw, H. E. Payne, & J. J. E. Hayes, 349+
 Laor, A. & Draine, B. T. 1993, *ApJ*, 402, 441
 Leroy, A., Bolatto, A., Stanimirović, S., Mizuno, N., Israel, F., & Bot, C. 2007, *ApJ*, 658, 1027
 Lynch, D. W. & Hunter, W. R. 1991, *Handbook of Optical Constants of Solids II*, ed. E. D. Palik (San Diego: Academic Press), 385–396
 Maiolino, R., Schneider, R., Oliva, E., Bianchi, S., Ferrara, A., Mannucci, F., Pedani, M., & Roca Sogorb, M. 2004, *Nature*, 431, 533
 Meikle, W. P. S., Mattila, S., Pastorello, A., Gerardy, C. L., Kotak, R., Sollerman, J., Van Dyk, S. D., Farrah, D., Filippenko, A. V., Höflich, P., Lundqvist, P., Pozzo, M., & Wheeler, J. C. 2007, *ApJ*, 665, 608
 Morgan, H. L., Dunne, L., Eales, S. A., Ivison, R. J., & Edmunds, M. G. 2003, *ApJ*, 597, L33
 Moseley, S. H., Dwek, E., Glaccum, W., Graham, J. R., & Loewenstein, R. F. 1989, *Nature*, 340, 697
 Nozawa, T., Kozasa, T., Habe, A., Dwek, E., Umeda, H., Tominaga, N., Maeda, K., & Nomoto, K. 2007, *ApJ*, 666, 955
 Nozawa, T., Kozasa, T., Tominaga, N., Sakon, I., Tanaka, M., Suzuki, T., Nomoto, K., Maeda, K., Umeda, H., Limongi, M., & Onaka, T. 2008, *ApJ*, 684, 1343
 Nozawa, T., Kozasa, T., Umeda, H., Maeda, K., & Nomoto, K. 2003, *ApJ*, 598, 785

- Omont, A., Cox, P., Bertoldi, F., McMahon, R. G., Carilli, C., & Isaak, K. G. 2001, *A&A*, 374, 371
- Pastorello, A., Smartt, S. J., Mattila, S., Eldridge, J. J., Young, D., Itagaki, K., Yamaoka, H., Navasardyan, H., Valenti, S., Patat, F., Agnoletto, I., Augusteijn, T., Benetti, S., Cappellaro, E., Boles, T., Bonnet-Bidaud, J.-M., Botticella, M. T., Bufano, F., Cao, C., Deng, J., Dennefeld, M., Elias-Rosa, N., Harutyunyan, A., Keenan, F. P., Iijima, T., Lorenzi, V., Mazzali, P. A., Meng, X., Nakano, S., Nielsen, T. B., Smoker, J. V., Stanishev, V., Turatto, M., Xu, D., & Zampieri, L. 2007, *Nature*, 447, 829
- Philipp, H. R. 1985, *Handbook of Optical Constants of Solids*, ed. E. D. Palik (San Diego: Academic Press), 749–763
- Piller, H. 1985, *Handbook of Optical Constants of Solids*, ed. E. D. Palik (San Diego: Academic Press), 571–586
- Pozzo, M., Meikle, W. P. S., Fassia, A., Geballe, T., Lundqvist, P., Chugai, N. N., & Sollerman, J. 2004, *MNRAS*, 352, 457
- Rasmussen, A. P., Behar, E., Kahn, S. M., den Herder, J. W., & van der Heyden, K. 2001, *A&A*, 365, L231
- Rho, J., Kozasa, T., Reach, W. T., Smith, J. D., Rudnick, L., DeLaney, T., Ennis, J. A., Gomez, H., & Tappe, A. 2008, *ApJ*, 673, 271
- Roche, P. F., Aitken, D. K., & Smith, C. H. 1993, *MNRAS*, 261, 522
- Roessler, D. M. & Huffman, D. R. 1991, *Handbook of Optical Constants of Solids II*, ed. E. D. Palik (San Diego: Academic Press), 919
- Rouleau, F. & Martin, P. G. 1991, *ApJ*, 377, 526
- Sasaki, M., Gaetz, T. J., Blair, W. P., Edgar, R. J., Morse, J. A., Plucinsky, P. P., & Smith, R. K. 2006, *ApJ*, 642, 260
- Sasaki, M., Stadlbauer, T. F. X., Haberl, F., Filipović, M. D., & Bennie, P. J. 2001, *A&A*, 365, L237
- Smith, J. D. T., Armus, L., Dale, D. A., Roussel, H., Sheth, K., Buckalew, B. A., Jarrett, T. H., Helou, G., & Kennicutt, Jr., R. C. 2007, *PASP*, 119, 1133
- Smith, N., Foley, R. J., & Filippenko, A. V. 2008, *ApJ*, 680, 568
- Stanimirović, S., Bolatto, A. D., Sandstrom, K., Leroy, A. K., Simon, J. D., Gaensler, B. M., Shah, R. Y., & Jackson, J. M. 2005, *ApJ*, 632, L103
- Sugerman, B. E. K., Ercolano, B., Barlow, M. J., Tielens, A. G. G. M., Clayton, G. C., Zijlstra, A. A., Meixner, M., Speck, A., Gledhill, T. M., Panagia, N., Cohen, M., Gordon, K. D., Meyer, M., Fabbri, J., Bowey, J. E., Welch, D. L., Regan, M. W., & Kennicutt, R. C. 2006, *Science*, 313, 196
- Sutherland, R. S. & Dopita, M. A. 1995, *ApJ*, 439, 381
- Todini, P. & Ferrara, A. 2001, *MNRAS*, 325, 726
- Tuohy, I. R. & Dopita, M. A. 1983, *ApJ*, 268, L11
- van Loon, J. T., Cioni, M.-R. L., Zijlstra, A. A., & Loup, C. 2005, *A&A*, 438, 273
- van Loon, J. T., Cohen, M., Oliveira, J. M., Matsuura, M., McDonald, I., Sloan, G. C., Wood, P. R., & Zijlstra, A. A. 2008, *A&A*, 487, 1055
- Williams, B. J., Borkowski, K. J., Reynolds, S. P., Blair, W. P., Ghavamian, P., Hendrick, S. P., Long, K. S., Points, S., Raymond, J. C., Sankrit, R., Smith, R. C., & Winkler, P. F. 2006, *ApJ*, 652, L33
- Wooden, D. H., Rank, D. M., Bregman, J. D., Witteborn, F. C., Tielens, A. G. G. M., Cohen, M., Pinto, P. A., & Axelrod, T. S. 1993, *ApJS*, 88, 477